Flow-induced vibration of a cantilevered cylinder in oscillatory flow at high KC

Otto E. Neshamar[1,*], Dominic A. van der A[1], Tom O'Donoghue[1]

School of Engineering, University of Aberdeen, Aberdeen, AB24 3UE, UK

Abstract

Flow-induced vibrations of a cantilevered circular cylinder are measured in sinusoidal, oscillatory, water flows with amplitude of reduced velocity in the range $1.9 \leq U_r \leq 4.4$ and Keulegan-Carpenter number in the range $120 \leq \mathrm{KC} \leq 900$ respectively. Flow velocities are measured using laser Doppler anemometry, and forces and moments are measured using a 6-axis load cell; the two-degree-of-freedom (2-DOF) cylinder motions are determined from the measured moments. The dominant type of vibration occurring within the flow half-period is shown to depend mainly on U_r, with predominantly in-line vibration occurring for $U_r \lessapprox 2.7$, figure-8 vibration occurring for $2.7 \lessapprox U_r \lessapprox 4$, and transverse vibration occurring for $U_r \gtrapprox 4$. In-line vibration frequency, f_x, is close to, or slightly higher than the cylinder's natural frequency in still-water, while transverse vibration frequency, f_y, is generally close to the vortex shedding frequency given by Strouhal number $\mathrm{St} = 0.2$. Some unsteadiness is seen in the transverse vibration frequency in that accelerating flow f_y is consistently higher than decelerating flow f_y for the same instantaneous reduced velocity u_r. The most notable unsteady effect is seen in the in-line vibration amplitude, A_x, which is much higher during flow deceleration than during flow acceleration; maximum A_x occurs at decelerating $u_r \approx 2$ for all three vibration types. Transverse vibration amplitude, A_y, increases with increasing u_r and shows only slight asymmetry between accelerating and decelerating flow. Experiments with the cylinder placed within a large array of similar cylinders with a spacing between cylinders of six cylinder diameters, show that cylinder vibrations within the array are more variable than those of the isolated cylinder, but exhibit similar average vibration amplitudes and frequencies as the isolated cylinder. An empirical model for unsteady in-line vibration based on theoretical considerations and the experimental data is presented. Model-predicted and measured in-line vibration amplitudes through the flow half-period show good agreement for in-line, figure-8 and transverse vibrations.

Keywords: Flow-induced vibration, Cantilevered cylinder, Fluid forces, Oscillatory flow

1. Introduction

Flow-induced vibrations (FIV) of cylinders are important in engineering applications ranging from the small-scale vibrations of heat exchanger tubes to the large-scale vibrations of risers in the marine environment. Reviews of

*Corresponding author

Email address: o.neshamar@abdn.ac.uk (Otto E. Neshamar)

the topic have been presented by Naudascher (1987), Blevins (1990), Sarpkaya (2004), Williamson and Govardhan (2004) and Sumer and Fredsøe (2006). The majority of studies have investigated FIV under steady flow conditions, for which the vibrations have near-constant amplitude and frequency, governed by the cylinder mass ratio m^* (mass of the vibrating cylinder/mass of the displaced fluid), the reduced velocity $u_r = u/f_n d$, the Reynolds number $\mathrm{Re} = ud/\nu$, the aspect ratio (AR = cylinder length/diameter) and the damping characteristics of the cylinder, where u is flow velocity, f_n is cylinder natural frequency in still fluid, d is cylinder diameter and ν is the fluid kinematic viscosity. For $10^2 < \mathrm{Re} < 10^5$ (Schlichting and Gersten, 2017), vortex shedding occurs with frequency $f_{vs} \approx 0.2u/d$ (i.e. Strouhal number $\mathrm{St} = f_{vs}d/u \approx 0.2$). The shedding induces a fluctuating transverse force on the cylinder with frequency f_{vs} and a fluctuating in-line force with frequency $2f_{vs}$; a cylinder with two degrees of freedom (2-DOF) can therefore undergo resonant flow-induced vibrations in both in-line and transverse directions.

Steady-flow experiments involving 2-DOF FIV of rigid, flexibly-mounted cylinders (Jauvtis and Williamson, 2003), rigid, pivoted cylinders (Flemming and Williamson, 2005; Cagney and Balabani, 2014), and flexible, cantilevered cylinders, vibrating in the first structural mode, with no coupling between x and y motions, (King et al., 1973; Pesce and Fujarra, 2000) have shown that FIV occurs when $1 < u_r < 10$. For $1 \lessapprox u_r \lessapprox 2.5$ (the "first instability region"), large-amplitude in-line vibrations can occur due to symmetric vortex shedding from the cylinder, a phenomenon termed "wake breathing" (Naudascher, 1987). Symmetric vortex shedding does not occur for flow past a stationary cylinder: it only occurs once the cylinder has already been set in motion by asymmetric shedding. Similar symmetric vortex-shedding phenomena have been observed in experiments involving forced, in-line oscillation of a cylinder in steady flow by Nishihara et al. (2005), and in experiments involving steady plus low-amplitude oscillatory flow past a stationary cylinder by Konstantinidis and Balabani (2007). The occurrence of large-amplitude in-line FIV due to wake breathing in the first instability region depends on Re. No wake breathing was observed in Konstantinidis et al.'s (2021) numerical simulations of in-line FIV of a flexibly-mounted cylinder for $u_r = 1.5 - 4.5$ and $\mathrm{Re} \leq 250$. Similarly, no wake breathing was observed by Flemming and Williamson (2005) during FIV experiments for a pivoted cylinder, conducted with constant $\mathrm{Re}/u_r = 110$ (i.e. $\mathrm{Re} < 300$ for $u_r < 2.5$), while Gurian et al. (2019), who conducted experiments with constant $\mathrm{Re}/u_r = 770$, only observed wake-breathing if the cylinder oscillation was initiated manually. The vibration amplitude typically reduces to a minimum around $u_r \approx 2.5$, and for $2.5 \lessapprox u_r \lessapprox 4$ (the "second instability region"), the motions are characterised by large-amplitude vibration in both the in-line and transverse directions, resulting in the cylinder following a "figure-8" trajectory. Konstantinidis (2014) described how the reduction in vibration amplitude between the first and second instability region is a consequence of asymmetric vortex shedding, as the timing of asymmetric vortex shedding relative to the cylinder motion can result in negative energy transfer from the fluid to the structure when $u_r \approx 2.5$. Experiments conducted by Aguirre (1978), summarised by Naudascher (1987), in which a splitter plate was placed in the wake of the cylinder in order to prevent asymmetric vortex-shedding, have shown that the plate prevents the amplitude reduction at $u_r \approx 2.5$. Instead, amplitudes remain high up to $u_r \approx 3$, after which the streamwise vibrations occur at lower amplitudes compared to those measured without a plate. Similar splitter-plate observations have been made by Okajima et al. (2004), who also investigated in-line

FIV of pivoted cylinders with a range of different aspect ratios. Okajima et al. (2004) showed that in-line FIV for cylinders with low aspect ratio (AR <= 10) form a single instability region in the range $1 < u_r < 4$, with no reduction in vibration amplitude at $u_r \approx 2.5$. For $4 \lessapprox u_r \lessapprox 10$, vibrations occur primarily in the transverse direction, often reaching amplitudes much higher than those observed for $u_r < 4$; FIV within this region has been explored by e.g. Jauvtis and Williamson (2003) for rigid, flexibly-mounted cylinders, and Pesce and Fujarra (2000) for cantilevered cylinders.

Comparatively less literature exists for FIV in oscillatory flow, defined by $u(t) = U\sin(2\pi t/T)$, where U is velocity amplitude and T is the flow period. The parameters that govern flow behaviour and FIV in oscillatory flow are the same as for steady flow with the addition of the Keulegan-Carpenter number $\mathrm{KC} = UT/d$. Oscillatory flow Reynolds number is given by $\mathrm{Re} = Ud/\nu$, while the reduced velocity is time-varying, $u_r(t) = u(t)/f_\mathrm{n}d$, with amplitude $U_r = U/f_\mathrm{n}d$. Other relevant parameters are the frequency ratio $f_r = f_\mathrm{n}/f$, where $f = 1/T$ is the flow frequency, the number of lift oscillations per flow period $n = f_\mathrm{L}/f$, where f_L is the fundamental lift frequency (obtained as the peak frequency in the power spectrum of measured lift force, see Sumer and Fredsøe, 2006), and the so-called Stokes or frequency parameter $\beta = \mathrm{Re}/\mathrm{KC} = d^2/\nu T$ (Sarpkaya, 2005). Vortex-shedding from a stationary cylinder in oscillatory flow is a function of KC: in flow visualisations conducted for $\beta = 255$ and $\beta = 730$, Williamson and Roshko (1988) observed distinct regimes of vortex-shedding, with no shedding below KC = 7, one pair of vortices shed when $7 < \mathrm{KC} < 15$, two vortex-pairs when $15 < \mathrm{KC} < 24$, and so on. Sumer and Fredsøe (2006) show that the increase of one in the number of vortex pairs for an increase of 8 in KC is consistent with St = 0.2 for oscillatory flow. Experimental studies of FIV in oscillatory flow are reviewed by Sumer and Fredsøe (2006); most involve 1-DOF, transverse-only oscillation of a flexibly-mounted cylinder, and results are generally presented as a function of KC, with vibration amplitudes and frequencies becoming similar to steady-flow FIV amplitudes and frequencies at high KC. A few studies have investigated 2-DOF FIV of flexibly-mounted cylinders in oscillatory flow, including Lipsett and Williamson (1994), who conducted 2-DOF FIV tests for $2 < \mathrm{KC} < 60$ and $1 < f_r < 9$. Lipsett and Williamson proposed three mathematical models for predicting 2-DOF vibrations: two uncoupled x and y models and a coupled model. Their models perform fairly well for low f_r; however, for $f_r > 4$, their experiments show increasingly complex 2-D vibration trajectories, as well as significant variations in FIV for different flow periods, neither of which are captured by their models. Similar observations were made in numerical simulations by Zhao (2013) for $10 < \mathrm{KC} < 40$ and $0.5 < f_r < 10$, where trajectories become increasingly complex for $f_r > 2$. To the authors' knowledge, only Fu et al. (2013) have conducted FIV experiments for high KC and reported vibration amplitudes through the flow period. Their experiments focused on the transverse (y) vibrations of a slender cylinder that was forced to oscillate in the x direction in still water, with $26 \leq \mathrm{KC} \leq 178$ and $4 \leq U_r \leq 7.9$ (for these experiments U and T are velocity amplitude and period of the imposed streamwise harmonic cylinder motion). Results from Fu et al. (2013) show that FIV in oscillatory flow differs significantly from that in steady flow. Even for very high KC, for which a quasi-steady behaviour might be expected, unsteady behaviour was observed, including a hysteresis effect whereby vibration amplitudes observed during cylinder deceleration are significantly higher than vibration amplitudes during cylinder

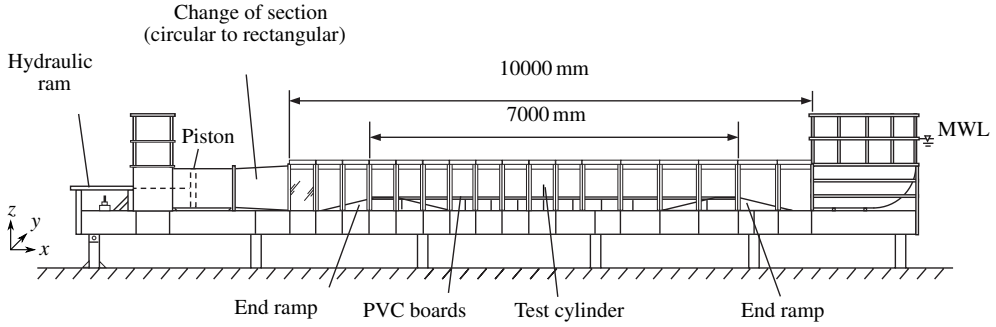

Figure 1: The Aberdeen Oscillatory Flow Tunnel

acceleration. Their results have been reproduced in subsequent numerical simulations by Thorsen et al. (2016) and by Fu et al. (2018), who were able to reproduce the time-dependent response characteristics of the cylinder.

The present paper reports on experiments conducted as part of a study of the hydrodynamic interactions between sea waves and submerged vegetation. Experiments were conducted in a large oscillatory water tunnel in which oscillatory flows with periods and amplitudes similar to the periods and amplitudes of oscillatory flows under full-scale waves can be generated. To build understanding of fundamental mechanisms, vegetation was represented by an array of small-diameter solid circular cylinders. The cylinders are mounted vertically in the tunnel, with one end fixed to the tunnel floor and the other end free. The combination of cylinder diameter, set-up and flow conditions results in a set of experiments in which cantilevered circular cylinders vibrate in the in-line and transverse directions in oscillatory flows under high-KC conditions. Section 2 describes the experimental set-up, test conditions and and data processing. Detailed experimental results for a single, isolated cylinder are presented and discussed in Section 3. Measurements of vibrations when the cylinder is contained within a uniform array of cylinders (representing a vegetation canopy) are presented in Section 4. In Section 5, an empirical model describing the unsteady characteristics of the in-line vibrations is presented and compared to the experimental results for the isolated cylinder. The main conclusions are presented in Section 6.

2. Experiments

2.1. Experimental conditions

The experiments were conducted in the Aberdeen Oscillatory Flow Tunnel (AOFT, Figure 1), which is capable of generating horizontal oscillatory flows with velocity amplitudes up to 1.5 m/s for periods of 5-10 s. The facility is a U-tube construction with a total length of 16 m, 10 m of which is a rectangular glass-sided test section, 0.75 m high and 0.3 m wide. For the present experiments a raised floor was present in the tunnel test section, consisting of a stainless steel frame covered with 25 mm thick PVC boards. The height of the raised floor was 0.25 m, reducing the internal height of the test section to 0.5 m. The 7 m long raised floor consisted of 12 separate boards, perforated with 8.5 mm-diameter holes to accommodate an array of cylinders. A load cell was built into one of the central boards

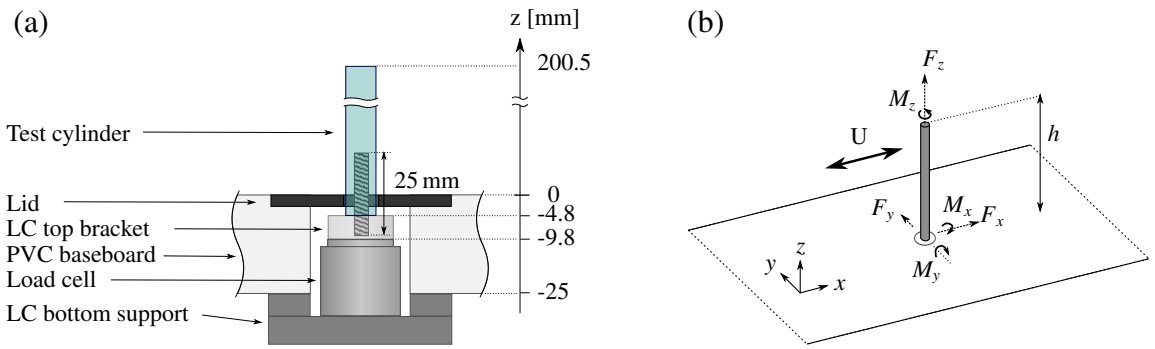

Figure 2: (a) Diagram of the load cell (LC) arrangement. (b) Definition sketch for axes, forces and moments.

for direct measurement of forces acting on a single cylinder. For the experiments discussed within the majority of this paper, a single, isolated cantilever cylinder was mounted on the load cell, and the rest of the test section bed was covered with acrylic tape, covering all the other holes to create a smooth bed. Results from subsequent experiments involving a full array of cantilever cylinders will be discussed in Section 4. The test cylinder consisted of solid PVC with a diameter of 8.3 mm and length of 205 mm. At its base, the cylinder was fitted with an M4 threaded stainless steel rod for attaching to the load cell. When installed, the height of the cylinder above the bed was measured to be 200.5 mm. A number of static-deflection tests were conducted on the cylinder, as well as free-vibration tests in air and in still water. Based on these tests, the Young's modulus E was determined to be 3.55-3.75 GPa. The cylinder natural frequency and damping ratio in air were $f_{\mathrm{air}} = 45.3$ Hz and $\zeta_{\mathrm{air}} = 0.01$. The corresponding values in still water were $f_{\mathrm{n}} = 33.9$ Hz and $\zeta_0 = 0.023$. The load cell was mounted on a stainless steel support located below the bed (Figure 2(a)), with a small steel bracket mounted to the front of the load cell, where the test cylinder can be attached. The whole installation was hidden underneath a 2 mm thick PVC lid to minimise water motion around the load cell. The test cylinder protruded through a hole in this lid with a 1 mm clearance around the cylinder, ensuring that the cylinder was solely supported by the load cell. Figure 2(b) shows the x, y, z coordinate system and the force and moment convention.

Forces and moments acting on the test cylinder were recorded using an ATI F/T Nano17 IP68 6-axis load cell, measuring at 1000 Hz. The load cell is used in three calibration settings with force sensing ranges of 12 N, 25 N and 50 N and moment sensing ranges of 120 N·mm, 250 N·mm and 500 N·mm, respectively; the corresponding force sensing resolutions are 1/320 N, 1/160 N and 1/80 N, and the moment sensing resolutions are 1/64 N·mm, 1/32 N·mm and 1/16 N·mm. Flow velocities were measured using a Dantec FibreFlow 2-component Laser Doppler Anemometer (LDA), operated in back-scatter mode. Velocities were recorded at a variable sampling rate, typically averaging between 100 - 200 Hz The LDA probe was mounted on a 3-axis computer-controlled traverse, allowing the x, y, and z-location of the measurement volume to be controlled with a resolution of 12.5 µm. For all test cases, the flow velocities were measured in the 'free-stream' approximately 100 mm above the top of the test cylinder.

Table 1: Experimental conditions. $T = 6$ s for all experiments; the last column indicates the dominant observed FIV regime (see Section 3.2).

U (m/s)	U_r	Re	KC	FIV regime
0.16	0.57	1326	120	No FIV
0.22	0.79	1838	166	No FIV
0.28	1.01	2359	212	No FIV
0.35	1.23	2865	259	No FIV
0.41	1.45	3387	305	No FIV
0.47	1.67	3911	352	No FIV
0.53	1.90	4431	398	In-line
0.60	2.12	4940	444	In-line
0.66	2.34	5472	491	In-line
0.72	2.57	6010	538	In-line
0.79	2.80	6548	585	Figure-8
0.85	3.03	7080	631	Figure-8
0.92	3.26	7608	679	Figure-8
0.98	3.48	8129	725	Figure-8
1.04	3.71	8660	772	Figure-8
1.11	3.93	9183	819	Figure-8
1.17	4.16	9705	865	Transverse
1.23	4.39	10248	913	Transverse

Experiments were conducted for 18 flow amplitudes ranging between $0.57 \leq U_r \leq 4.39$ (Table 1), all involving sinusoidal flow with a constant flow period of $T = 6$ s, corresponding to a constant frequency ratio of $f_r = f_n T = 203.4$ and a constant frequency parameter $\beta = \mathrm{Re}/\mathrm{KC} = 11.5$. This value is much lower than β-values of previous oscillatory flow experiments (Kühtz, 1996) because of the small-diameter cylinder and relatively large flow period in the present study. For each flow amplitude, the load cell calibration setting was selected to achieve optimal resolution while remaining within the moment sensing range; the 12 N setting was used for $0.57 \leq U_r \leq 2.34$, the 25 N setting was used for $2.57 \leq U_r \leq 3.48$ and the 50 N setting was used for $3.71 \leq U_r \leq 4.39$. For experiments involving a single, isolated cylinder in the centre of the tunnel test section, flow velocities are spatially uniform, with the exception of the low-velocity region in the wake of the cylinder and the boundary layers at the tunnel floor, walls and ceiling. Fredsøe and Deigaard (1992) give the following empirical relation for estimating the boundary layer thickness in sinusoidal flow over a smooth bed:

$$\frac{\delta}{a_w} = 0.086\mathrm{Re}_w^{-0.11}, \tag{1}$$

where $a_w = UT/2\pi$ is the flow orbital amplitude, and $\mathrm{Re}_w = Ua_w/\nu$ is the orbital amplitude based Reynolds number. For the present experiments, this indicates a near-bed boundary layer thickness between 10-20 mm, and, since the lower part of the cantilever cylinder is stationary, the flow is considered to be both vertically and horizontally uniform. To verify the boundary layer estimate, a vertical profile of $u(z, t)$ was measured for $U = 0.53$ m/s and showed vertically uniform velocities down to $z = 10$ mm, below which the velocity magnitude decayed to zero with proximity to the bed. Root-mean-square (RMS) turbulent fluctuations in the free-stream were between 1-1.5% of the flow amplitude.

2.2. Data processing

LDA and load cell data was collected for a duration of 50-100 flow periods. Measurements were separated into individual flow periods based on a once-per-cycle digital trigger signal, sent from the piston control software at the start of each flow period, and recorded by the LDA and load cell data acquisition systems. Ensemble-averaged quantities are calculated using:

$$\langle\theta(t)\rangle = \frac{\sum_{n=1}^{N} \theta(t + (n-1)T)w(t + (n-1)T)}{\sum_{n=1}^{N} w(t + (n-1)T)} \qquad 0 \leq t < T, \tag{2}$$

where θ is any variable to be averaged, angle brackets denote the ensemble-average, t is time within the flow period and N is the total number of flow periods recorded. $\theta(t)$ is the value of the variable at time t, and $w(t)$ is a weighting factor applied to θ at time t. The irregularly-sampled LDA data were averaged by applying a 'binning' method, where each 6 s flow period was divided into 300 bins of duration $\Delta t = 1/50$ s, and each velocity measurement is assigned to its given bin. Within each bin, velocity samples are weighted by the particle residence time (Buchhave et al., 1979). Since the LDA sample rate is proportional to the number of seeding particles passing through the measurement volume, sample rates are high at high velocity and low at the flow zero-crossings. The regularly-sampled load cell data are uniformly weighted, i.e. $w = 1$ for all t.

The forces acting on the test cylinder can be separated into low-frequency and high-frequency components. The low-frequency forces are associated with the fundamental frequency of the oscillatory flow ($f = 0.167\,\mathrm{Hz}$), while the high-frequency forces related to FIV are within 10-50 Hz. Due to the large difference between f and f_n, the low-frequency forces are easily isolated by applying a low-pass filter with a 5 Hz cut-off. The ensemble-averaged forces and moments are calculated from the low-pass filtered data using Equation (2). Analysis of the high-frequency vibrations was performed by applying a continuous wavelet transform (CWT) to the measured moment data. While the high-frequency vibrations can be detected by both the force and moment measurements, only the moment data are used here because of the better signal-to-noise ratio. The CWT of a time-varying function $\theta(t)$ is given by:

$$W_\psi(\theta, a, b) = \frac{1}{a^{1/2}} \int_{-\infty}^{\infty} \theta(t) \cdot \mathrm{conj.} \left[\psi \left(\frac{t-b}{a} \right) \right] \mathrm{d}t, \tag{3}$$

where a is a series of scale factors, each of which is mapped to an 'equivalent' frequency, b is the translation of the wavelet along t, and 'conj.' denotes the complex conjugate. The mother wavelet ψ used in the present analysis is a Morse wavelet with parameters (γ, P) = (3, 120), and calculations were performed using the built-in `cwt` function in MATLAB R2018a. For each experiment, the CWTs of M_x and M_y were evaluated for each flow period. For a given translation b, the scale factor a which produces a peak value of $\left|W_\psi\right|$ corresponds to the approximate vibration frequency at time $t = b$, and the corresponding value of W_ψ contains the vibration amplitude and phase. The sequence connecting successive peaks of $\left|W_\psi\right|$ at each b forms the 'wavelet ridge', and a better-resolution estimate of the instantaneous vibration frequency is obtained by measuring the rate of change in phase along the wavelet ridge (Wang et al., 2013). Instantaneous frequency is evaluated through the following forward-difference expression based on Feldman (2011):

$$f(t) = \frac{1}{\Delta t} \arctan \left[W_{\psi R}(t) \cdot \mathrm{conj.} \left(W_{\psi R}(t + \Delta t) \right) \right], \tag{4}$$

where Δt is the sampling interval $(1000\,\mathrm{Hz})^{-1}$, and $W_{\psi R}(t)$ is the complex value of the wavelet ridge at translation $b = t$. The forward-difference method introduces some noise spikes, which are removed by applying a median filter of order 10. The wavelet-obtained frequencies and amplitudes of vibration through each flow period were subsequently ensemble-averaged by applying Equation (2). Amplitudes were averaged with uniform weighting, while frequencies were weighted by signal amplitude, and any values below 5 Hz were excluded in order to remove any influence of the low-frequency signal.

Cylinder tip deflections are calculated from measured moments using Euler-Bernoulli beam theory, with the assumption that deflections remain small and elastic, and contain the linear sum of a quasi-static deflection (related to the flow frequency) and a FIV-related dynamic deflection. Since vibration amplitudes remain relatively small, and occur at frequencies close to the first natural frequency, dynamic deflections are assumed to occur solely in the first flexural mode, with the deflection shape resembling the first eigenmode of a uniform cantilever in free, undamped vibration (e.g. Strømmen, 2014). Taking into account that the load cell records moments at $z = -10\,\mathrm{mm}$, and that the cylinder is mounted to the top bracket at $z = -5\,\mathrm{mm}$, the dynamic tip deflection is calculated from the dynamic

(high-pass filtered) moment by:

$$X(t) = \frac{0.2752L^2}{EI} M'_y(t), \tag{5a}$$

$$Y(t) = -\frac{0.2752L^2}{EI} M'_x(t), \tag{5b}$$

where L is the cylinder length (measured from the base at $z = -5$ mm), E is Young's modulus, I is second moment of area, and where M'_x, M'_y are high-frequency (FIV-related) moments recorded by the load cell. Note that due to the sign convention used, deflection in the y-direction causes a negative moment M_x (see Figure 2(b)), which is why there is a minus sign in Equation (5b). Similarly, vibration amplitudes obtained from CWT are converted to tip deflection amplitudes:

$$A_x(t) = \frac{0.2752L^2}{EI} \left| W_\psi(M_y, a_{\max}, t) \right|, \tag{6a}$$

$$A_y(t) = \frac{0.2752L^2}{EI} \left| W_\psi(M_x, a_{\max}, t) \right|, \tag{6b}$$

where $a_{\max}$ denotes the scale factor where $\left|W_\psi\right|$ is highest, equivalent to the frequency of vibration. Calculated deflections showed good agreement with visual observations and are assumed to be accurate within some small uncertainty.

3. Results

3.1. Force and moment results

Figure 3 shows example measured M_y and M_x for a single flow oscillation for four velocity amplitudes. The M_y results for $U_r = 1.45$ show low-frequency forcing corresponding to f, while the other three cases show high-frequency FIV-related moments superimposed on the low-frequency forcing; in M_x, only high-frequency forcing is present. Force measurements were recorded as well as moments, although measurements of F_x for $U_r < 2.34$ were discarded due to poor data quality caused by the low force. For all experiments with $U_r \geq 2.34$, the low-pass filtered and ensemble-averaged F_x closely matched M_y in shape, and the ratio $M_{y,\mathrm{RMS}}/F_{x,\mathrm{RMS}}$ was 120±5 mm, slightly higher than the theoretical ratio of 115 mm for a cantilever with $h = 200$ mm that is uniformly loaded from its free end to 20 mm from the fixed end (the 20 mm being the sum of an estimated 10 mm boundary layer, where velocities and loading are very low, and the 10 mm vertical distance from $z = 0$ to the front of the load cell). Based on the very consistent $M_{y,\mathrm{RMS}}/F_{x,\mathrm{RMS}}$ obtained for experiments with $U_r \geq 2.34$, the low frequency F_x for all experiments is determined by dividing the measured low-frequency M_y by 120 mm.

In the absence of FIV, the instantaneous horizontal force on a cylinder in oscillatory flow is given by the Morison equation:

$$F_x = \frac{1}{2}\rho C_D dh \cdot u\,|u| + (1 + C_\mathrm{a})\frac{\rho\pi d^2 h}{4}\dot{u}, \tag{7}$$

where C_D and C_a are empirical drag and added mass coefficients. Note that the cylinder vibration leads to a separate added-mass (see Section 5); to differentiate between them, the 'flow-frequency added-mass' is written C_a while the

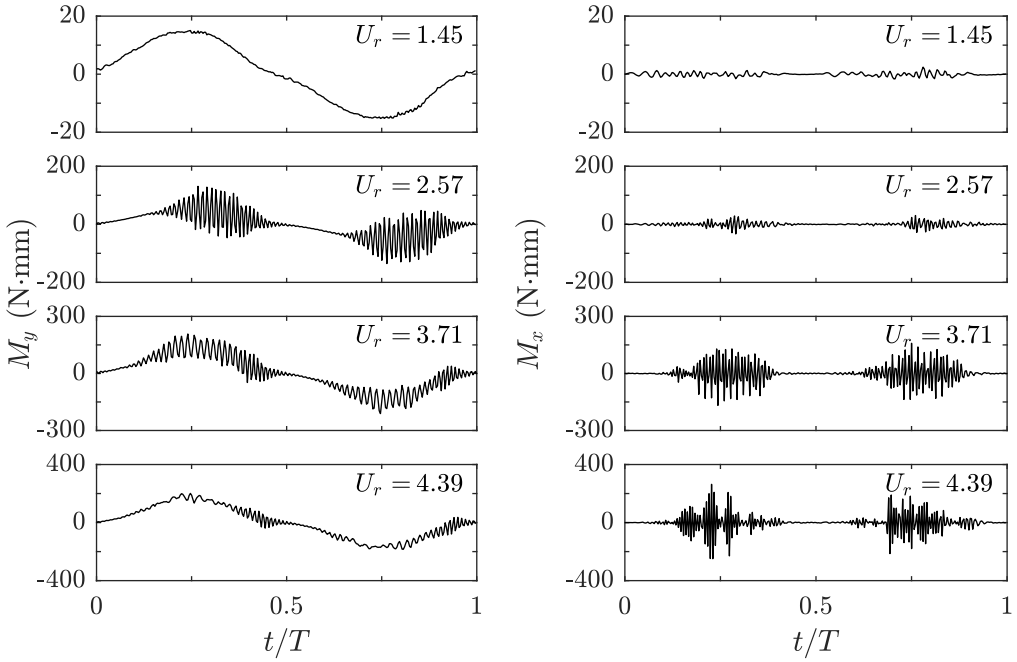

Figure 3: Example measured M_y and M_x for one flow period for four experiments.

'vibration added-mass' is written C_A. For the present experiments, drag and added-mass coefficients were obtained by fitting Equation (7) to the low-frequency force (i.e. the low-pass filtered, ensemble-averaged M_y divided by 120 mm) and velocity measurements using a least-squares method; the results for C_D and C_a are shown in Figure 4. Since KC is very high for these experiments, the drag force dominates, and, as a result, the least-squares estimate of C_a can vary significantly with small differences in force or velocity. To quantify this sensitivity, the shaded area in the figures indicate values of C_D and C_a that vary within 10% of the best fit: the results show that the uncertainty in C_D is much less than that for C_a. To the authors' knowledge, C_D and C_a values corresponding to the very high KC and low β values of the present experiments have not been previously reported. Sarpkaya (1976) measured forces on cylinders in a wide range of oscillatory flow conditions, reaching KC = 200 for β = 497 (the lowest value tested). Sarpkaya's results show C_D steadily reducing from 2 to 1.3 for $20 < KC < 200$, while $C_a \approx 0.2$. While the present measurements of C_D are consistent with Sarpkaya's results, the measured C_a values are significantly higher. The reason for this discrepancy, which is present over the full range of test conditions regardless of FIV, is not clear. Possible causes may include 3-D flow features caused by the cantilever geometry, such as cylinder tip vortices occurring at flow reversal; future experiments involving flow visualisation are needed to investigate this further. The present low-β, high-KC results can also be compared to steady-flow results, for which $C_D \approx 1$ for the range of Re of the experiments (Schlichting and Gersten, 2017); this is consistent with the present results. The dependence of C_D on U_r observed in Figure 5 correlates with the FIV behaviour described in Section 3.2, as FIV results in increased drag for both in-line and transverse vibration (e.g. Tanida et al., 1973), especially for 2-DOF vibration (Sarpkaya, 1995). As shown in

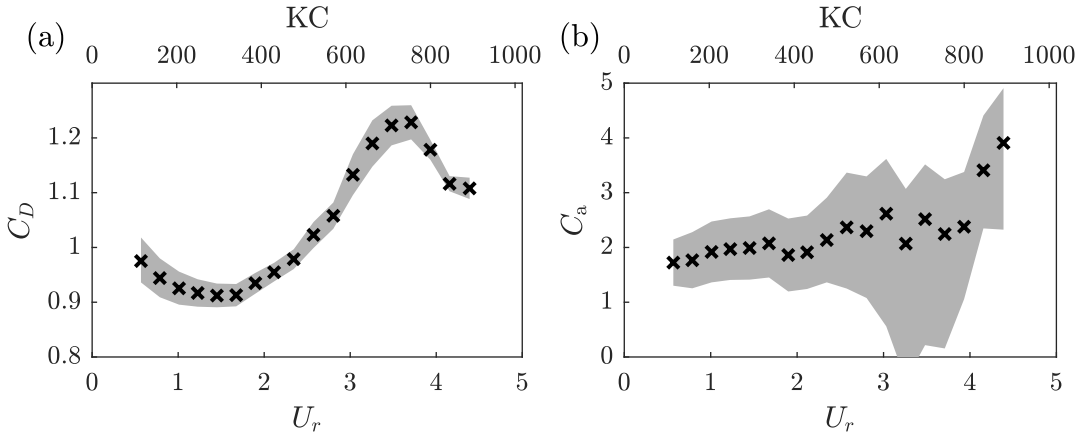

Figure 4: Drag and added-mass coefficients obtained by least-squares fitting.

Section 3.2, there are three main regimes of cylinder vibration: the in-line regime, which occurs for $1.90 \leq U_r \leq 2.57$; the figure-8 regime, which occurs for $2.80 \leq U_r \leq 3.93$; and the transverse regime, which occurs for $4.16 \leq U_r \leq 4.39$. The increase in C_D at $U_r > 1.8$ in Figure 4 corresponds to the onset of the in-line vibrations, the highest C_D occurs when the cylinder undergoes fig-8 vibrations, and C_D decreases as the cylinder vibrations become transverse.

The cylinder deflection due to low-frequency forcing can be estimated with quasi-static analysis. An approximation of the tip deflection is obtained by assuming uniform loading over the total cylinder length L, with a distributed force equal to F_x/h; then, quasi-static tip deflection along x is given by (Budynas and Nisbett, 2015):

$$X_0(t) = \frac{L^4}{8EI}\frac{F_x(t)}{h}, \tag{8}$$

where $F_x(t)$ is given by Equation (7), which closely describes the measured low-frequency forces. Hence, the time-varying $X_0(t)$ for any of the present experiments can be obtained by applying Equations (7) and (8) with C_D and C_a from Figure 4. The amplitude of the low-frequency tip deflection, as a function of U_r, is obtained by combining Equations (7) and (8) (for high KC, the impact of C_a on the maximum force is negligible):

$$\frac{X_{0,\max}}{d} = \frac{L^4}{8EI}\frac{1}{2}\rho C_D d U^2 \approx 0.0106 C_D U_r^2, \tag{9}$$

which can be evaluated directly for each flow amplitude using the U_r and C_D-values shown in Figure 4. Amplitudes of low-frequency deflection for all experiments are shown for comparison in Figure 14, which also shows the amplitudes of the high-frequency vibrations along x and y, which are the main focus of this work. Amplitudes of low-frequency and high-frequency motions have similar magnitude and low-frequency amplitudes increase with U_r, as predicted by Equation (9). The highest quasi-static deflection of $X_{0,\max} = 0.22d$ occurs for $U_r = 4.39$, validating the assumption that quasi-static deflection remains small at all times, as discussed in Section 2.2.

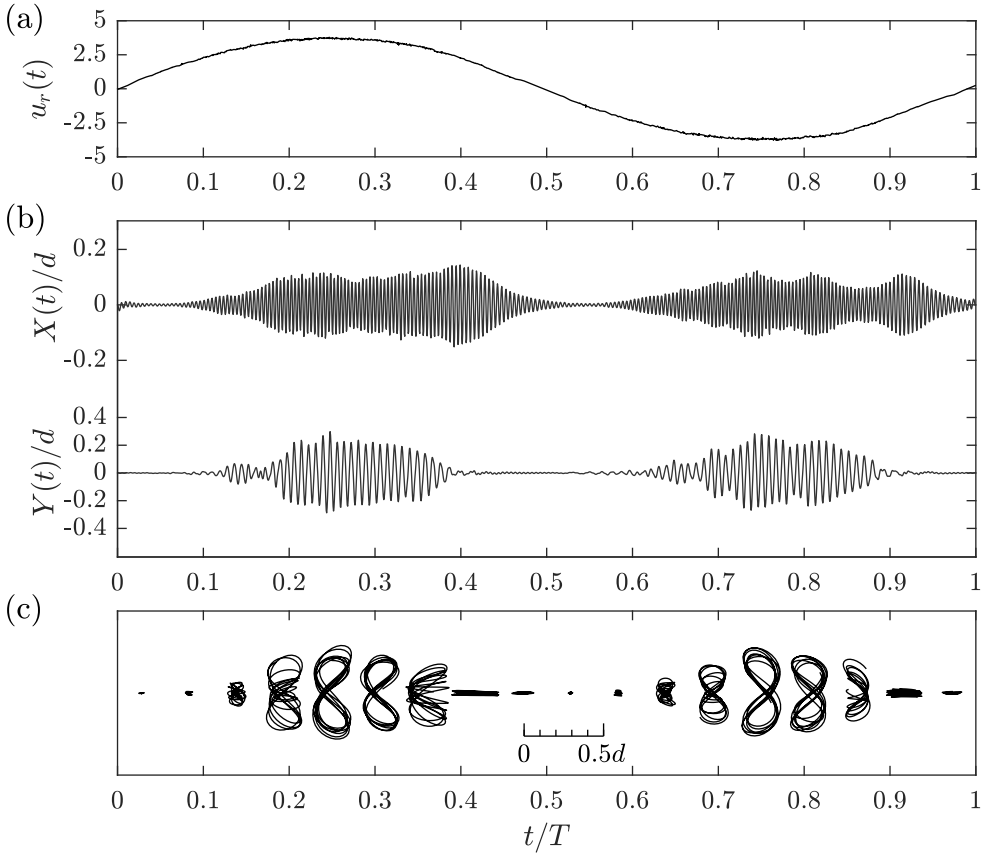

Figure 5: Example vibration results for $U_r = 3.71$: (a) $u_r(t)$ for a single example flow period, (b) $X(t)$ and $Y(t)$ for the example flow period, (c) vibration trajectories throughout the example flow period. Trajectories are shown in 1:1 aspect ratio, at the scale shown in the figure.

3.2. Vibration trajectories

Figure 5 shows the measured dynamic cylinder tip deflections, $X(t)$ and $Y(t)$, for a sample flow period with $U_r = 3.71$. The flow velocity is shown in Figure 5(a), and $X(t)$ and $Y(t)$ are shown in Figure 5(b). For this experiment, Figure 5(c) shows $Y(t)$ plotted against $X(t)$ within 18 time intervals of 0.3 s ($t/T = 0.05$) duration, illustrating the vibration trajectories occurring throughout the flow period. For this experiment, Figure 5(c) shows figure-8 vibrations developing gradually as flow velocity increases, transitioning to in-line vibrations around $t/T \approx 0.35$, before ceasing to vibrate at $t/T = 0.5$; similar behaviour is observed in the subsequent flow half-period (animated vibration trajectories for three example flow periods at $U_r = 2.57$, 3.71 and 4.39 are included in the online supplementary material). With the exception of occasional chaotic fluctuations, the vibrations in the second flow half-period are identical to those of the first half-period. This was the case for all experiments, and so, measurements from the second half-period were combined with measurements from the first half-period, effectively doubling the size of the dataset.

For each flow condition, the vibrations exhibited a degree of chaotic fluctuations. Unpredictable vibrations were

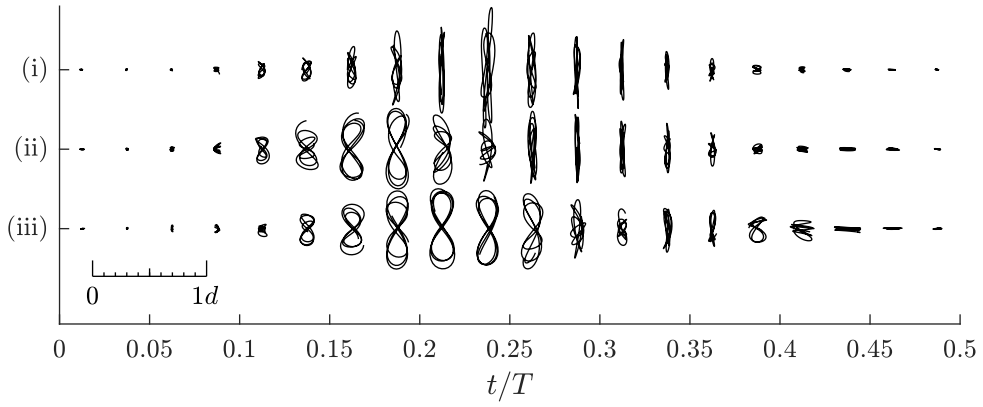

Figure 6: Vibration trajectories for three sample flow half-periods for $U_r = 4.39$.

also observed in oscillatory flow experiments by Lipsett and Williamson (1994). As an example, Figure 6 shows a comparison of vibrations observed in three sample half-periods for $U_r = 4.39$. Sequence (i) shows the behaviour most commonly seen for this velocity, i.e. transverse vibration dominance; sequence (ii) initially develops figure-8 motions, which transition to matching sequence (i) at $t/T > 0.25$; and sequence (iii) is dominated by figure-8 motions and only becomes similar to sequence (i) at $t/T > 0.45$. The different trajectory sequences observed in different half-periods of the same experiment can be grouped together in distinct 'trajectory sequence categories'; for this purpose, a method of quantifying similarity between two trajectory sequences is applied. The method is based on comparing vibration amplitudes A_x and A_y through individual half-periods (obtained from the wavelet transform, see Section 2.2), and defining the similarity of vibrations between two half-periods by the cosine similarity of vibration amplitudes in x, y (Cha, 2007):

$$s_x(i,j) = \frac{\sum_{t=1}^{N_s} A_{x,i}(t) A_{x,j}(t)}{\sqrt{\sum_{t=1}^{N_s} A_{x,i}^2(t) \sum_{t=1}^{N_s} A_{x,j}^2(t)}}, \qquad i,j = 1, \ldots, 2N, \tag{10a}$$

$$s_y(i,j) = \frac{\sum_{t=1}^{N_s} A_{y,i}(t) A_{y,j}(t)}{\sqrt{\sum_{t=1}^{N_s} A_{y,i}^2(t) \sum_{t=1}^{N_s} A_{y,j}^2(t)}}, \qquad i,j = 1, \ldots, 2N, \tag{10b}$$

where $s_x(i,j)$ denotes the cosine similarity between half-periods i and j along the x-direction, $A_{x,i}(t)$ is the x-amplitude of vibration through half-period i, N_s is the number of samples within a half-period, and $2N$ is the total number of half-periods for the given flow condition. The cosine similarity between two amplitude sequences produces a value between 0 and 1, where 1 denotes perfect similarity in 'shape'. By defining a threshold value s_c (0.95 was used in the present analysis), two half-periods i and j can be grouped together in a common 'sequence category' if $s_x(i,j)$ and $s_y(i,j)$ are both greater than s_c. According to this categorisation, for example, case (i) in Figure 6 is representative for 83% of the half-periods for the $U_r = 4.39$ flow condition, while cases (ii) and (iii) account for only 4% and 1% of half-periods, respectively. Figure 7 shows results of the classification when applied to all flow half-periods for all 12

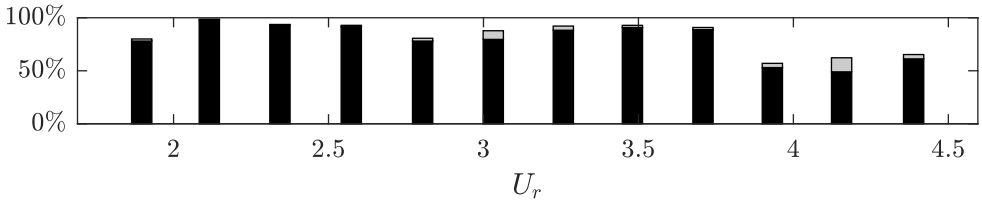

Figure 7: Percentage of half-periods in the largest (black) and second-largest (light grey) trajectory sequence category.

experiments where FIV occurred, showing only the percentages for the two largest sequence categories. The figure shows that there is always a single, clearly predominant trajectory sequence for a given flow amplitude.

Figure 8 presents an overview of the measured vibration trajectories through the flow half-period for all experiments. For each of the 12 experiments for which significant FIV occurred, the most-common 'trajectory sequence' through the flow half-period is shown as a horizontal sequence at the given U_r. The colour shading in the figure indicates regions of the diagram where the vibration type (in-line, figure-8, transverse) is the same. These regions are obtained by applying the following criteria to the normalised amplitudes $A_x^* = A_x/d$ and $A_y^* = A_y/d$ through each half-period: if $A_x^*(t)$ and $A_y^*(t)$ are less than 0.03 $\Rightarrow$ low vibration; if $A_x^*(t) \geq 0.03$ and $A_x^*(t) > 2A_y^*(t) \Rightarrow$ in-line vibration; if $A_y^*(t) \geq 0.03$ and $A_y^*(t) > 4A_x^*(t) \Rightarrow$ transverse vibration; and for any other case $\Rightarrow$ figure-8 vibration. For each $(U_r, t/T)$, the percentages of half-periods for which low vibration, in-line vibration, figure-8 vibration and transverse vibration occurred were calculated and denoted Φ_{Lo}, Φ_{IL}, Φ_{F8} and Φ_{Tv} respectively. The vibration type at each $(U_r, t/T)$ is classified as 'in-line', 'figure-8' or 'transverse' if Φ_{IL}, Φ_{F8} or Φ_{Tv} exceed 60% (note that, while the threshold is 60%, percentages are often close to 100%); the remaining points are classified as 'transitional' where Φ_{Lo} is less than 50%, and classified as 'low vibration' otherwise; Φ-values are interpolated along U_r to complete the shading in Figure 8. Dotted contour lines of constant $u_r(t)$ are labelled on the upper x-axis of Figure 8.

The sequences in Figure 8 can be divided into three 'FIV regimes' based on U_r: The 'in-line regime' ($1.90 \leq U_r \leq 2.57$), dominated by in-line vibrations, which develop near maximum velocity, reach a maximum vibration amplitude near $t/T = 0.3$, and gradually reduce as flow decelerates; the 'figure-8 regime' ($2.80 \leq U_r \leq 3.93$), where figure-8 vibrations first develop, before transitioning to in-line vibration during flow deceleration; and the 'transverse regime' ($4.16 \leq U_r \leq 4.39$), where transverse vibrations are dominant, occurring near peak velocity and transitioning to in-line vibration during flow deceleration. The sequence with $U_r = 2.80$, at the transition between in-line and figure-8 regimes, involves significantly lower vibration amplitudes than the sequences before and after. This is similar to the reduction between in-line and figure-8 regions observed in steady-flow studies (e.g. Cagney and Balabani, 2014), and is likely caused by competition between symmetric and asymmetric vortex-shedding modes (Gurian et al., 2019). The boundaries of the coloured regions in Figure 8 partially follow the contours of instantaneous reduced velocity $u_r(t)$, and the following approximate delineations can be observed: for $1 < u_r(t) < 2.5$, vibrations are either low-amplitude (during flow acceleration) or in-line (at peak velocity and during flow deceleration); for $2.5 < u_r(t) < 4$, vibrations

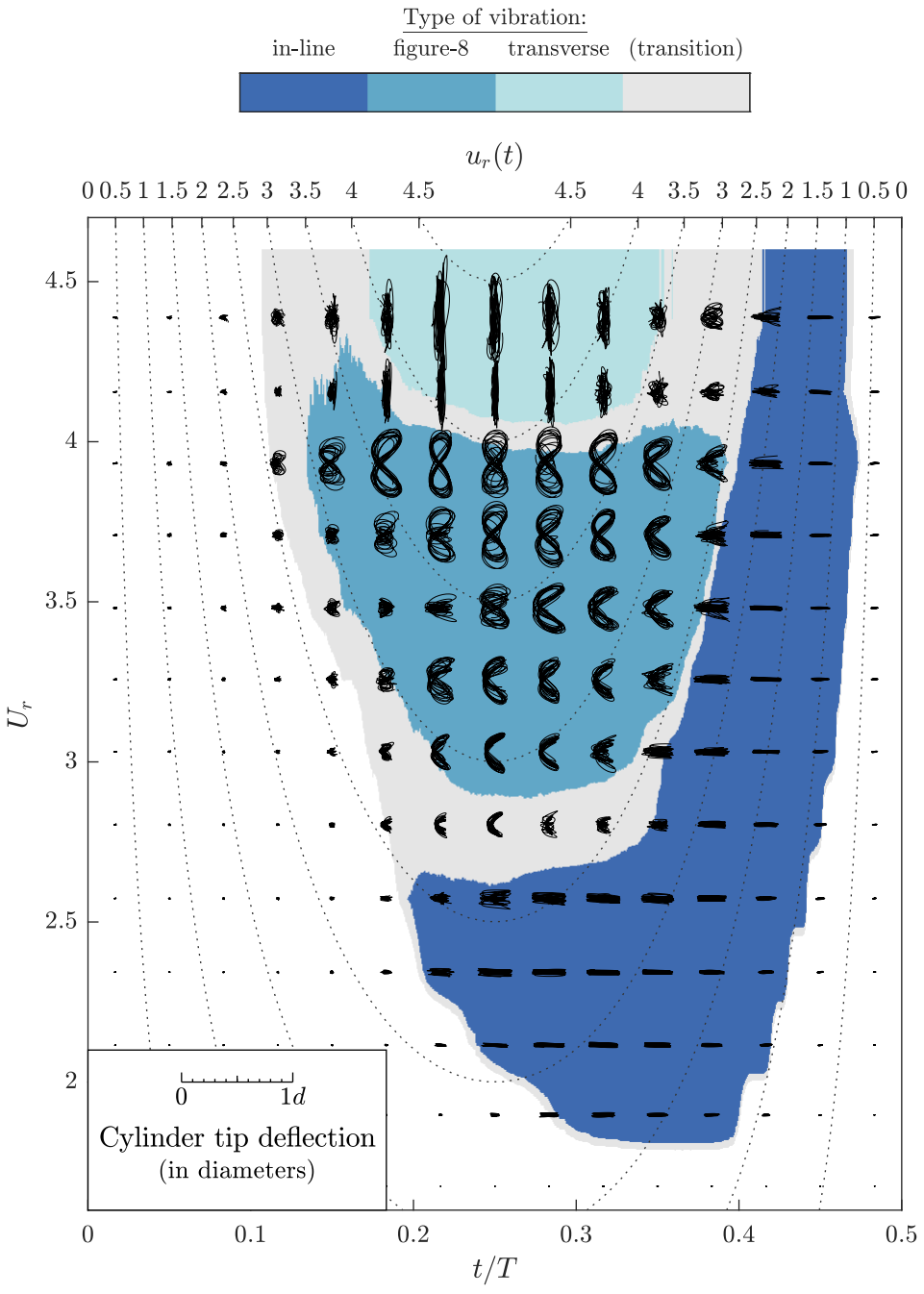

Figure 8: Vibration trajectories through the flow half-cycle at each U_r. Dotted contour lines are labelled on the upper x-axis and show instantaneous $u_r(t)$, and coloured regions indicate the predominant vibration type in accordance with the legend at the top.

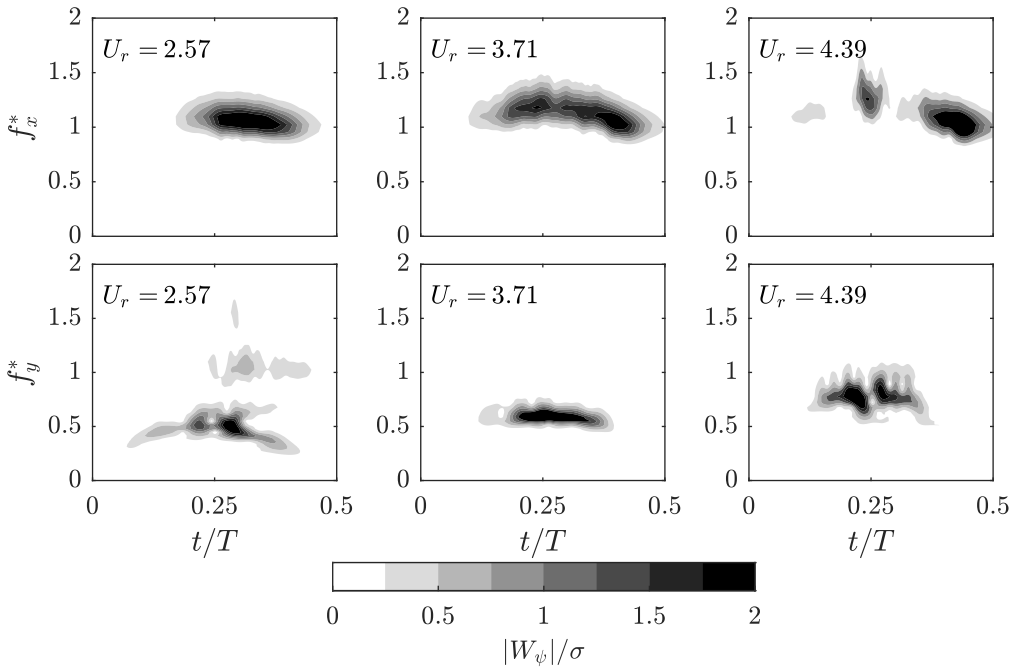

Figure 9: Example wavelet scalograms.

are figure-8 or transitional (and occasionally transverse for $U_r > 4$); and for $u_r(t) > 4$, vibrations are consistently transverse. These ranges of $u_r(t)$ are similar to the regions of in-line, figure-8 and transverse vibration observed in steady-flow studies (e.g. Jauvtis and Williamson, 2004, for a flexibly-mounted cylinder), indicating that the vibration type at a given time mainly depends on $u_r(t)$. Figure 8 consistently shows asymmetry between the accelerating flow ($0 < t/T < 0.25$) and decelerating flow ($0.25 < t/T < 0.5$) of the half-period, especially for the regions of in-line vibration, demonstrating that the characteristics of vibration are unsteady and depend on vibration history as well as on $u_r(t)$.

3.3. Vibration frequencies

Figure 9 shows example wavelet scalograms of the cylinder deflection in the x and y-directions through sample flow half-periods for $U_r = 2.57, 3.71$ and 4.39, representative of the in-line, figure-8 and transverse regimes. Each figure shows the magnitude of the wavelet transform normalised by the standard deviation of $X(t)$ or $Y(t)$ over the half-period, with frequencies normalised by the still-water natural frequency ($f_x^* = f_x/f_n$, $f_y^* = f_y/f_n$). For $U_r = 2.57$ and $U_r = 3.71$, Figure 9 shows the dominant vibrations occurring with $f_x^* \approx 1.1$ and $f_y \approx f_x^*/2$, while, for $U_r = 4.39$, vibrations occur with $f_x^* \approx 1.1$ and $f_x^* \approx 0.8$; all of these frequencies are consistent with those observed for in-line, figure-8 and transverse vibration of cylinders in steady flow for $2 < u_r < 4.5$ (Jauvtis and Williamson, 2004). The transverse vibrations for $U_r = 2.57$ exhibit multi-frequency characteristics with two separate 'wavelet ridges', with the primary ridge near $f_y^* = 0.5$ and a secondary ridge at $f_y^* \approx 1$. The location of the secondary ridge coincides with large-

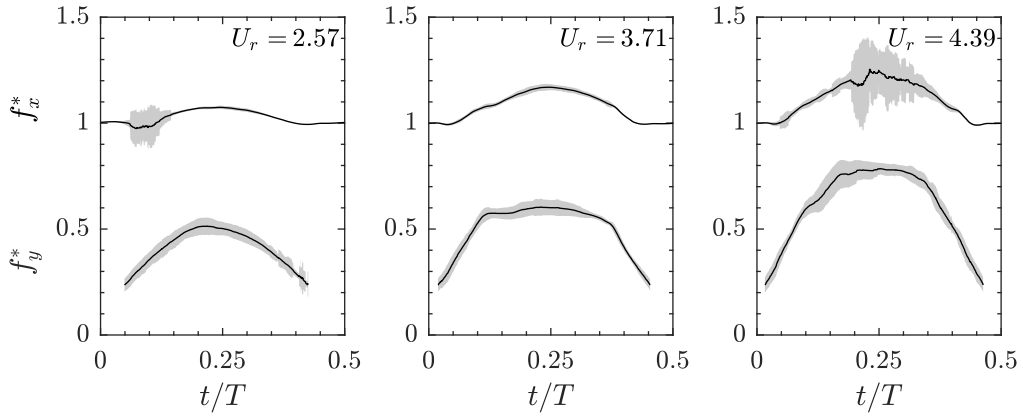

Figure 10: Ensemble-averaged vibration frequencies f_x^* and f_y^*, with the shaded area showing standard deviations.

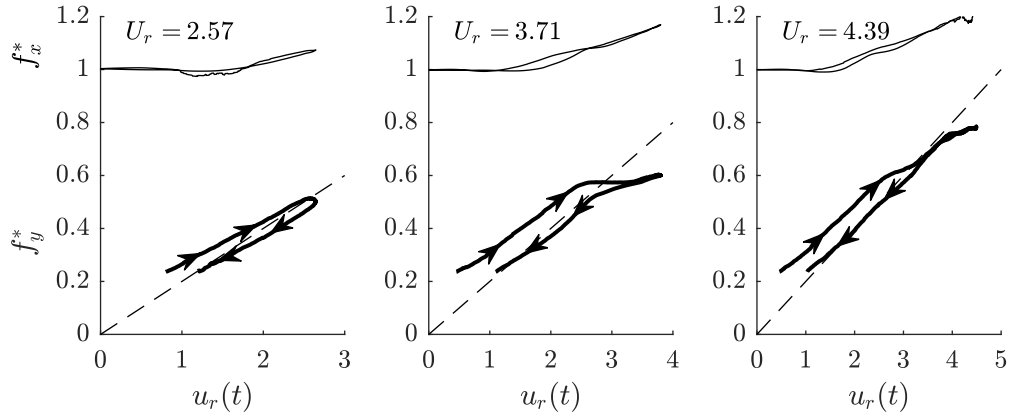

Figure 11: Frequency against $u_r(t)$ for (a) U_r = 2.57, (b) U_r = 3.71 and (c) U_r = 4.39.

amplitude vibrations in f_x^*, indicating that it represents a small transverse component of the in-line vibration. Figure 10 shows ensemble-averaged f_x^* and f_y^* for three flow cases, with ±1 standard deviation shown as grey areas. Frequency measurements are generally very consistent, as shown by the narrow standard deviations. For U_r = 2.57, the region of increased standard deviation occurs when the vibration amplitude is close to zero, and vibration frequency is therefore uncertain. For U_r = 4.39, f_x becomes significantly more uncertain near peak velocity due to the predominantly transverse vibrations (see Figure 8). Figure 11 shows the same ensemble-averaged frequencies as in Figure 10, now plotted against $u_r(t)$, with arrows added to f_y^* to indicate the path of f_y^* through the flow half-period, and with the dashed line representing $f_{\mathrm{St}}^* = f_{\mathrm{St}}/f_{\mathrm{n}}$ based on St = 0.2. The results show that f_x^* follows approximately the same path during flow acceleration and deceleration for the 3 experiments; this was the case for all 12 experiments for which significant FIV occurred. The results for the transverse vibration frequencies are more complicated: for U_r = 2.57, f_y is higher than f_{St} during flow acceleration and slightly below f_{St} during deceleration. For U_r = 3.71, f_y is higher than

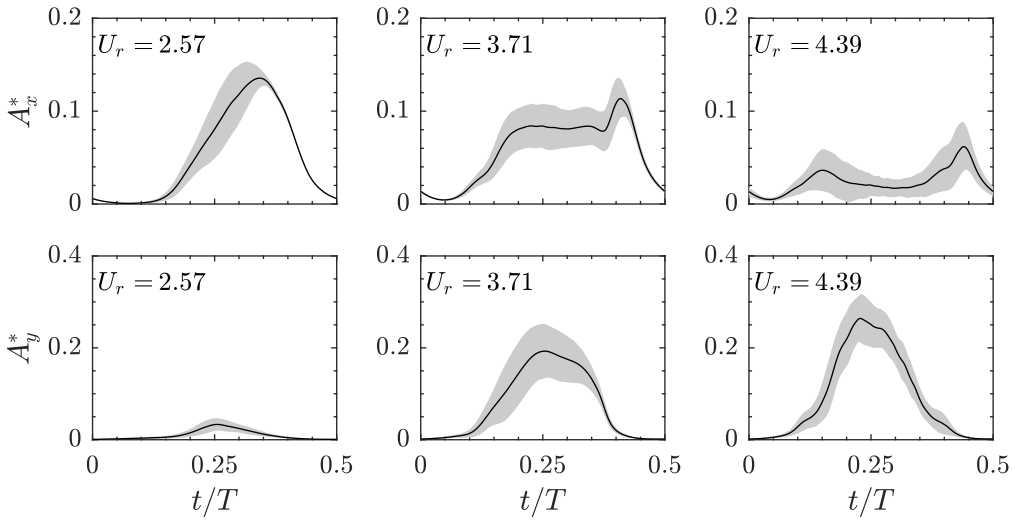

Figure 12: Ensemble-averaged vibration amplitudes A_x^* and A_y^*, with the shaded area showing standard deviations.

f_{St} until $u_r(t) \approx 3$, while for higher $u_r(t)$, vibrations in x and y are synchronised at $f_y^* = f_x^*/2$; During flow deceleration, $f_y \simeq f_{\mathrm{St}}$ for velocities below $u_r(t) \approx 3$. For $U_r = 4.39$, f_y is again higher than f_{St} during acceleration until $u_r(t) \approx 3$. For $u_r(t) > 3$, f_y^* is close to but slightly lower than f_{St}, and, as for $U_r = 3.71$, $f_y \simeq f_{\mathrm{St}}$ during deceleration for velocities less than $u_r(t) \approx 3$.

The results presented in Figure 11 are representative of results from all experiments that resulted in significant FIV. Present observations share similarities with results from flow visualisations by Cagney and Balabani (2014), who, for a pivoted cylinder undergoing 2-DOF FIV in steady flow, reported that the vortex-shedding frequency f_{vs} follows St ≈ 0.2 for $0.5 < u_r/f_x^* < 2$, where in-line vibrations occur, after which, synchronisation occurs, with $f_{\mathrm{vs}} = f_x/2$ for $2 < u_r/f_x^* < 3$, where figure-8 vibrations occur, followed by f_{vs} becoming greater than $f_x/2$ for $u_r/f_x^* > 3$, where transverse vibrations begin to develop (Cagney and Balabani, 2014, did not report measured values of f_x^*, but stated that it varies with u_r). The main feature that distinguishes the present oscillatory flow FIV from steady flow FIV is the asymmetry in f_y^* between the accelerating and decelerating stages of the flow half-period for $u_r(t) < 3$, where f_y^* is consistently higher than f_{St} during flow acceleration and close to f_{St} during flow deceleration.

3.4. Vibration amplitudes and phases

Figure 12 shows ensemble-averaged tip vibration amplitudes for the same three experiments shown in Figures 9, 10 and 11, with the grey areas representing ±1 standard deviation. For the examples shown, the peak value of A_x^* is highest for $U_r = 2.57$ (the in-line vibration regime) and reduces with increasing U_r, whereas the peak value of A_y^* is lowest for $U_r = 2.57$ and increases with increasing U_r. In general, standard deviations are large when vibrations are growing and small when vibrations are decaying, as seen most strikingly in A_x^* for $U_r = 2.57$. For the figure-8-dominant case, $U_r = 3.71$, the largest variability is seen in A_y^*, for which the standard deviation reaches a maximum

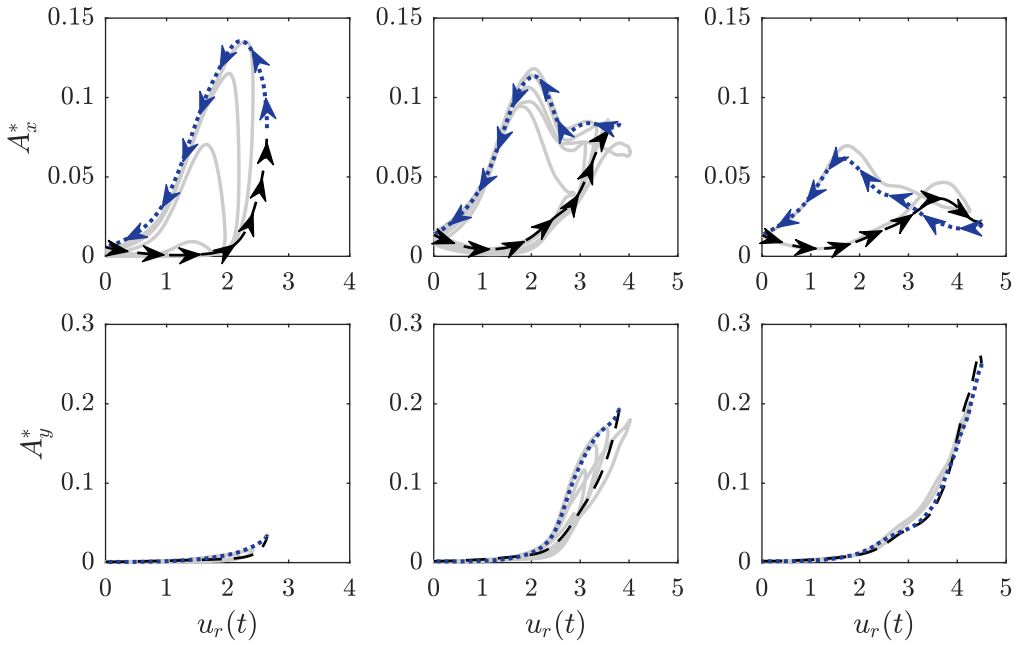

Figure 13: Ensemble-averaged vibration amplitudes for (left) in-line-dominant vibration ($1.90 \leq U_r \leq 2.57$), (middle) figure-8-dominant vibrations ($2.80 \leq U_r \leq 3.93$), and (right) transverse-dominant vibrations ($4.16 \leq U_r \leq 4.39$)

value of 0.07. Similar to the in-line-dominant case with $U_r = 2.57$, the variation is greatest as vibrations grow during flow acceleration and the variation becomes very small later in the flow half-period as the flow decelerates and the vibrations decay in amplitude. For $U_r = 4.39$, which has the largest vibration amplitudes, the standard deviations are slightly lower than for the figure-8 case, with a maximum value of 0.06, indicating that the variability of vibration amplitude gradually reduces with increasing U_r.

Figure 13 shows the ensemble-averaged A_x^* and A_y^* plotted against $u_r(t)$ for all experiments. The left column presents the experimental results for which the FIV is inline-dominant; the middle column presents the results for the figure-8-dominant experiments, and the results for the transverse-dominant experiments are shown in the right column. The results corresponding to the three 'representative' cases - $U_r = 2.27$, 3.71 and 4.39 - are shown as black and blue arrowed lines, where black corresponds to the flow acceleration stage of the half-period and blue corresponds to the deceleration stage. The figure shows that vibration amplitudes along x are very different for the three FIV regimes. For the inline-dominant cases, the vibration amplitude is very low for much of the accelerating stage of the flow; A_x^* then increases rapidly as $u_r(t)$ approaches and passes maximum velocity, before gradually decaying to zero as the flow further decelerates. For the figure-8 cases, A_x^* behaves similarly to the in-line cases, but with a short 'flat section' after peak velocity where A_x^* remains nearly constant. When velocity drops below $u_r(t) = 2.7$, the vibration transitions to in-line vibration, and A_x^* increases to a peak at $A_x^* \approx 0.12$ before decreasing to zero as the flow further decelerates. For the transverse-dominant cases, A_x^* slowly increases with increasing $u_r(t)$ until $u_r \approx 3.9$, after which A_x^* reduces

as purely transverse vibrations develop. After peak velocity, A_x^* slowly increases, reaching a peak at $u_r \approx 1.9$, where vibration is purely in-line, before reducing to zero as the flow further decelerates. In contrast to the in-line vibration amplitudes, the transverse vibration amplitudes show similar behaviour for the three FIV regimes: A_y^* increases as $u_r(t)$ increases, reaches a peak at maximum u_r, and decreases as $u_r(t)$ decreases, more-or-less following the same path as for the accelerating stage. The transverse vibration amplitudes exhibit much less asymmetry than the in-line amplitudes, which means that $A_y^*(t)$ depends primarily on flow velocity. Some transverse asymmetry or 'hysteresis' occurs in the figure-8-dominant cases, for which A_y^* is higher during deceleration than during acceleration. This hysteresis occurs over the range of $u_r(t)$ where the 'flat section' in the A_x^*-plot occurs, which is also the range of u_r where frequencies are synchronised at $f_y^* = f_x^*/2$ (Figure 11), indicating that these three effects are linked and are related to the figure-8 motion. The most striking feature in Figure 13 is the strong hysteresis in A_x^* between accelerating and decelerating parts of the flow half-period. The hysteresis in A_x^* can be related to the 'wake-breathing' mechanism described by Naudascher (1987). Wake-breathing is a motion-induced phenomenon, where the in-line oscillation of the cylinder produces symmetric vortex-shedding as well as the periodic widening and narrowing of the wake, resulting in an unsteady in-line force which grows in proportion to A_x^*. Since A_x^* is very small during flow acceleration, the 'wake-breathing force' remains small; however, once large-amplitude oscillations develop, the wake-breathing force becomes much more significant, and results in much larger A_x^* during flow deceleration. It is worth noting that the asymmetric behaviour in A_x^* and near-symmetric behaviour in A_y^* are the opposite to what was observed for the vibration frequencies (Figure 11), with f_x^* being reasonably symmetric and f_y^* showing asymmetry between the acceleration and deceleration stages of the flow half-period.

Comparing the measured A_x^*, A_y^* to existing literature poses a challenge, as no previous experiments involving a cantilevered or pivoted cylinder in horizontal oscillatory flow are known to the authors. Instead, Figure 14 shows present values of peak amplitude $A_{x,\max}^*$, $A_{y,\max}^*$, plotted against $U_r/f_{x,\max}^*$, together with A_x^*, A_y^* measurements from two steady-flow studies: Cagney and Balabani (2014), involving 2-DOF FIV of a pivoted cylinder with $m^* = 2.7$ and $\mathrm{Re}/u_r = f_\mathrm{n} d^2/\nu \approx 1400$ for $0.5 < u_r/f_x^* < 3.5$; and Pesce and Fujarra (2000), involving transverse FIV of a cantilevered cylinder with $m^* = 2.36$ and $\mathrm{Re}/u_r \approx 1900$ for $3 < u_r < 16$ (for the latter, the cylinder was apparently capable of 2-DOF motion, but only A_y^* was reported by the authors). For reference, the present experiments were conducted with $m^* = 1.4$ and $\mathrm{Re}/U_r = 2335$. In Figure 14, A_x^* and A_y^* represent the oscillation amplitude at the cylinder tip for pivoted as well as for cantilevered cylinders. U_r in Figure 14 is normalised by f_x^* in order to remove the effect of differences in m^*, as recommended by Khalak and Williamson (1999); since f_x^* was not reported by Pesce and Fujarra (2000), estimates of f_x^* are obtained using the model presented in Section 5 (applying Equation 14b with $C_2 = 3.5$). For comparison purposes, Figure 14(a) includes the amplitude of low-frequency deflection, as previously discussed in Section 3.1. Figure 14(a) shows that A_x^*-values reported by Cagney and Balabani (2014) are similar in magnitude to the present results, with similar variation in A_x^* with u_r/f_x^*. For $U_r/f_{x,\max}^* < 2$, measured $A_{x,\max}^*$ is significantly lower than for steady-flow results; this may indicate that for $U_r/f_{x,\max}^* < 2$, the rate of increase in A_x^* is too slow to reach 'steady-state' A_x^*-values within the flow half-period. Above $U_r \approx 2$, values of $A_{x,\max}^*$ for the present

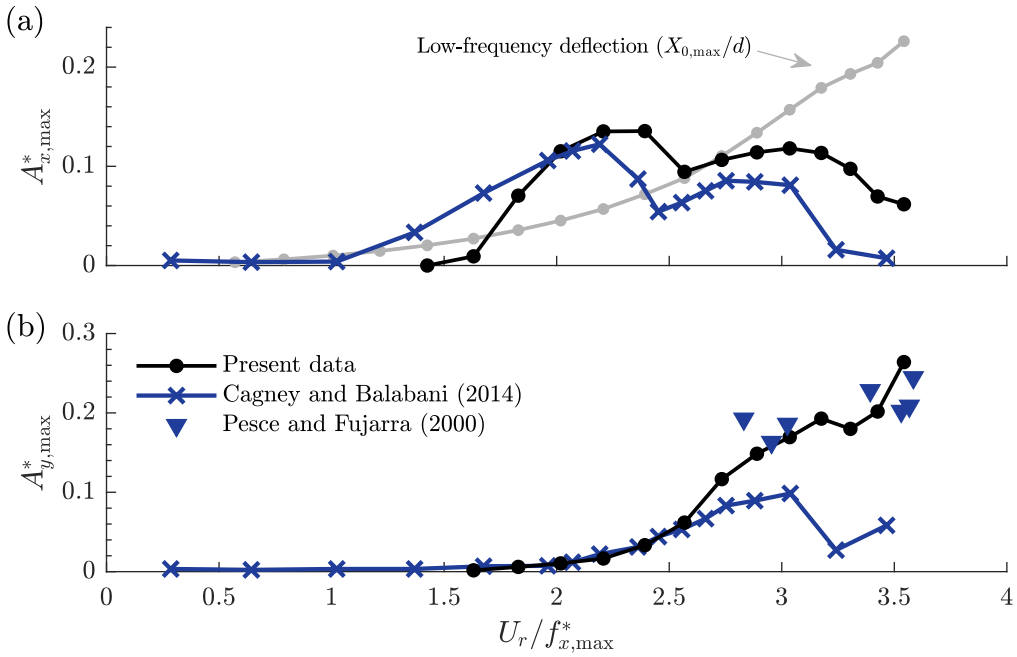

Figure 14: Comparison of $A_{x,\max}, A_{y,\max}$ from present experiments with A^*_x, A^*_y values from steady flow experiments. For comparison, (a) includes the low-frequency deflection determined from Equation (9).

results are higher than the values reported by Cagney and Balabani (2014). This is a consequence of the unsteady flow: for these conditions, Figure 13 shows that, regardless of U_r, the peak value of A^*_x occurs when $u_r(t) \approx 1.9$ during deceleration. Hence, all of the present $A^*_{x,\max}$-values shown in Figure 14(a) relate to vibration in the 'in-line' range of $u_r(t)$. Figure 14(b) shows that results for A^*_y by Pesce and Fujarra (2000), for $3 < u_r/f^*_x < 3.6$, closely match the present measurements. Results for A^*_y by Cagney and Balabani (2014) closely match the present results for $U_r/f^*_{x,\max} \lessapprox 2.6$, above which, their results are significantly lower than present measurements and the results of Pesce and Fujarra (2000); the reason for this difference is unclear, and it may be caused by differences between the pivoted-cylinder and cantilever set-ups. The difference may also be related to the lower value of Re/u_r in the experiments of Cagney and Balabani (2014): for transverse FIV with $u_r > 4$, Govardhan and Williamson (2006) have shown that maximum A^*_y increases with Re, and a similar increase in A^*_y with Re may be expected for $u_r < 4$.

When the cylinder is vibrating in a figure-8 pattern (generally for $2.5 < u_r < 4$), its motion can be approximated as a Lissajous curve (Flemming and Williamson, 2005), with displacements given by:

$$X(t) = A_x \sin(2\pi f_x t + \phi_{xy}), \tag{11a}$$

$$Y(t) = A_y \sin(\pi f_x t), \tag{11b}$$

where ϕ_{xy} denotes the phase difference between the x and y displacement, and where, due to synchronisation during figure-8 motion, we have $f_y = f_x/2$. The value of ϕ_{xy} was calculated for each individual flow period from the

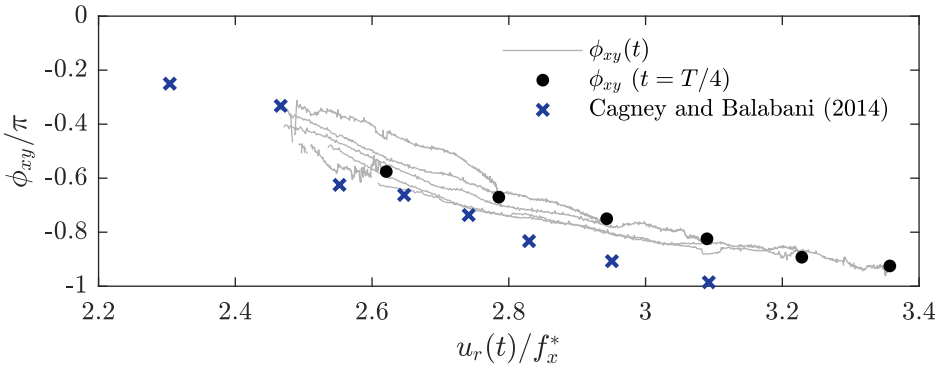

Figure 15: Lissajous phase during figure-8 vibrations.

phase information in the wavelet-transformed moment data, and was subsequently ensemble-averaged (removing outliers) to produce the average Lissajous phase for each phase in the flow half-period where figure-8 motion occurred. Ensemble-averaged values of ϕ_{xy} at peak velocity as well as during flow deceleration are shown in Figure 15, where results are compared to results from the steady-flow pivoted-cylinder experiments by Cagney and Balabani (2014). Figure 15 does not include any values of ϕ_{xy} during flow acceleration, as the ϕ_{xy}-values during flow acceleration were highly variable, and consistent ensemble-averages could not be obtained. At peak velocity, ϕ_{xy} becomes more stable and consistent between flow periods, and it remains reasonably consistent during flow deceleration until vibrations transition to in-line motion. As Figure 15 shows, average values of ϕ_{xy} fall along a common curve, indicating ϕ_{xy} to be mainly velocity dependent. The dependence of ϕ_{xy} on u_r from the present experiments is in reasonable agreement with results from Cagney and Balabani; the differences in magnitude of ϕ_{xy} may be due to the differences between the present cantilevered-cylinder set-up and their pivoted-cylinder set-up.

4. Flow-induced vibration of a cylinder within an array

An additional experiment was conducted in which the test cylinder was placed within an array of cylinders. In addition to load-cell measurements and free-stream flow velocity measurements, vertical profiles of flow velocity were also measured with the LDA for selected flow velocity amplitudes. FIV for steady flow through an array has been the subject of significant investigation due to its importance in the design of nuclear reactor components (Païdoussis, 1983). FIV in an array is influenced by the relative array spacings S_x/d and S_y/d (illustrated in Figure 16(b)). Vortex-shedding within staggered arrays with $S_x/S_y = 0.87$ was investigated by Oengören and Ziada (1998), who reported that St ≈ 0.2 for $S_y/d > 5$, with St increasing as S_y/d reduces. More recently, Zhao et al. (2015) performed 2-D simulations of transverse FIV of an array of 36 cylinders in a square, 6-by-6 arrangement with $S/d = 1.5 - 5$. They found that FIV depends on the position of a cylinder within the array: for $S/d = 5$, 'upstream' cylinders exhibited FIV similar to an isolated cylinder, while the cylinders at the end of the array had higher peak vibration amplitudes, occurring at higher u_r compared to the isolated cylinder case. Jiang et al. (2016) performed experiments involving

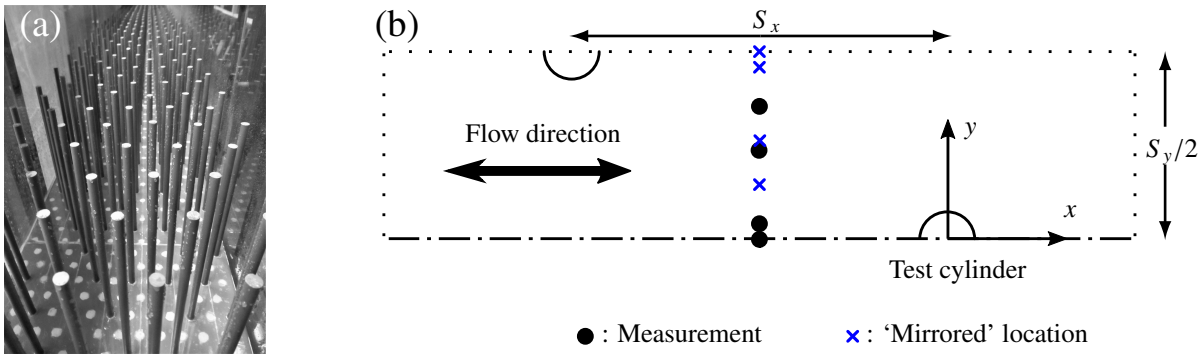

Figure 16: (a) Cylinder array within the AOFT test section. (b) Overview of x, y coordinates where velocity profiles were measured (plan view). The dashed line at the bottom indicates symmetry, and the dotted lines at the sides and top indicate periodic boundaries.

2-DOF FIV of a flexibly-mounted cylinder in a uniform, staggered array of stationary cylinders with $S_x/S_y = 0.87$ and $S_y/d = 2.5$, and observed FIV occurring for $1.5 < u_r < 10$, with several general similarities to FIV of an isolated cylinder. Each of these studies involved steady flow through cylinders spanning the full height of the water column; to the authors' knowledge, no previous studies have investigated FIV of submerged arrays of cantilevers, in either steady or oscillatory flow.

The array used in the present experiments is shown in Figure 16(a). The cylinders were of the same PVC material used for the test cylinder, had height $h \approx 205$ mm and diameter $d = 8$ mm, and were arranged in a staggered pattern with a centre-to-centre spacing of $S_x = S_y = 48$ mm ($S_x/d = S_y/d = 6$). The periodic geometry is illustrated in Figure 16(b), which also shows the four x, y locations where vertical profiles of flow velocity were measured. With the exception of the test cylinder, all other cylinders in the array were mounted by inserting with tight fit into 24 mm-deep holes drilled into the raised floor. All cylinders in the array vibrated under flow conditions, but only the vibrations of the test cylinder were measured. The array had a length of 7 m, and the test cylinder was located approximately in the middle. Initial flow velocity measurements in the wider region around the test cylinder showed that flow near the cylinder is fully-developed and minimally influenced by the side walls, indicating that the cylinder can be modelled as being positioned within an infinite, uniform array. Measurements of forces, moments and free-stream velocities were recorded for 18 flow conditions ($T = 6$ s, 0.16 m/s $< U_\infty <$ 1.56 m/s, where U_∞ is 'free-stream' flow amplitude), and detailed flow velocity profiles were recorded for 5 selected flow conditions. Due to the geometric symmetry of the array and the symmetry between the two half-periods of the oscillatory flow, the measurements at the four positions represented by the black dots in Figure 16(b) can be mirrored to give measurements at the four mirrored positions represented by the blue x's in the figure; the vertical profile of horizontal velocity can then be averaged over the height of the array to produce the spatially-averaged in-array horizontal velocity $\langle u \rangle (x = S_x/2, z, t)$.

A '2-layer' model for predicting vertically-averaged in-array flow velocities $\hat{u}(t)$ from the known above-array

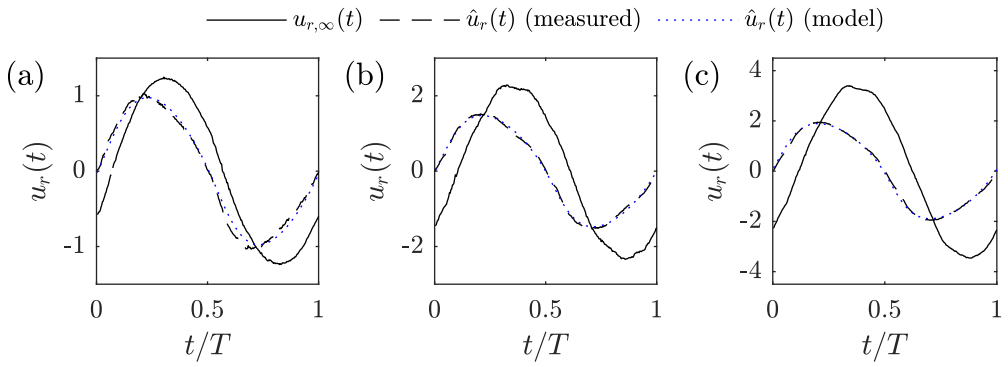

Figure 17: Measured and model-predicted in-array velocity for three experiments, $U_{r,\infty}/\hat{U}_r$ = (a) 1.24/1.03, (b) 2.26/1.59, and (c) 3.58/2.07.

free-stream velocity, $u_\infty(t)$, is given by Lowe et al. (2005):

$$\frac{\partial(\hat{u}-u_\infty)}{\partial t} = \frac{|u_\infty|u_\infty}{L_s} - \frac{|\hat{u}|\hat{u}}{L_d} - \left(\frac{(1+C_\mathrm{a})\lambda_p}{1-\lambda_p}\right)\frac{\partial\hat{u}}{\partial t} \tag{12}$$

where $L_s = 2h/C_f$ and $L_d = 2h(1-\lambda_p)/(C_D\lambda_f)$ are characteristic length scales of shear and drag, C_D and C_a are cylinder drag and added-mass coefficients, and C_f is a friction coefficient parameterising the shear force at the top of the array. Array geometry is parameterised using $\lambda_f = A_f/A_T$ and $\lambda_p = A_p/A_T$, where A_f is the frontal area of a cylinder ($d\times h$), A_p is the plan area of a cylinder and A_T is floor area per cylinder (overall floor area divided by number of cylinders). Equation (12) is a nonlinear ordinary differential equation (ODE) that is solved for $\hat{u}(t)$ using the `ode45` function in MATLAB R2018a. Equation (12) assumes that velocities within the array are vertically uniform, and that forces acting on each cylinder are governed by the Morison equation (Equation 7). The value of C_D for array flow differs from the isolated-cylinder value (Lowe et al., 2005); for the five experiments in which the detailed in-array velocities were measured, taking $C_\mathrm{a} = 1$, C_D was determined by a least-squares fit between the ensemble-averaged measured moments and the 'reconstructed moment' $M_{y,r}$, obtained from the numerically integrated Morison equation:

$$M_{y,r}(t) = \frac{1}{2}\rho C_D d\int_0^h \langle u\rangle|\langle u\rangle|\cdot(z+z_0)\mathrm{d}z + (1+C_\mathrm{a})\frac{\rho\pi d^2}{4}\int_0^h \langle\dot{u}\rangle\cdot(z+z_0)\mathrm{d}z \tag{13}$$

where $z_0 = 10$ mm is the distance from the load cell to $z = 0$. The result was $C_D \simeq 1.75 \pm 0.1$ for all five experiments. The in-array velocities, $\hat{u}(t)$, for all 18 experimental cases were then determined from Equation 12 with $C_D = 1.75$, $C_\mathrm{a} = 1$ and $C_f = 0.02$ (Lowe et al., 2005), and the in-array reduced velocities were calculated as $\hat{u}_r(t) = \hat{u}(t)/f_\mathrm{n}d$. Figure 17 shows examples of the measured and Equation (12)-predicted in-array velocities, showing excellent agreement in terms of velocity amplitude, phase and shape. Experiments were conducted for 'free-stream' reduced velocity amplitudes of $0.58 < U_{r,\infty} < 5.46$, resulting in 'in-array' reduced velocity amplitudes of $0.53 < \hat{U}_r < 2.74$.

Figure 18 shows examples of the vibration trajectories through four individual flow periods for the cylinder within the array for $\hat{U}_r = 2.62$. While the general vibration behaviour resemble that observed for the isolated cylinder case (Section 3.2), including in-line motions as well as figure-8 motion, the trajectories appear more chaotic and can differ

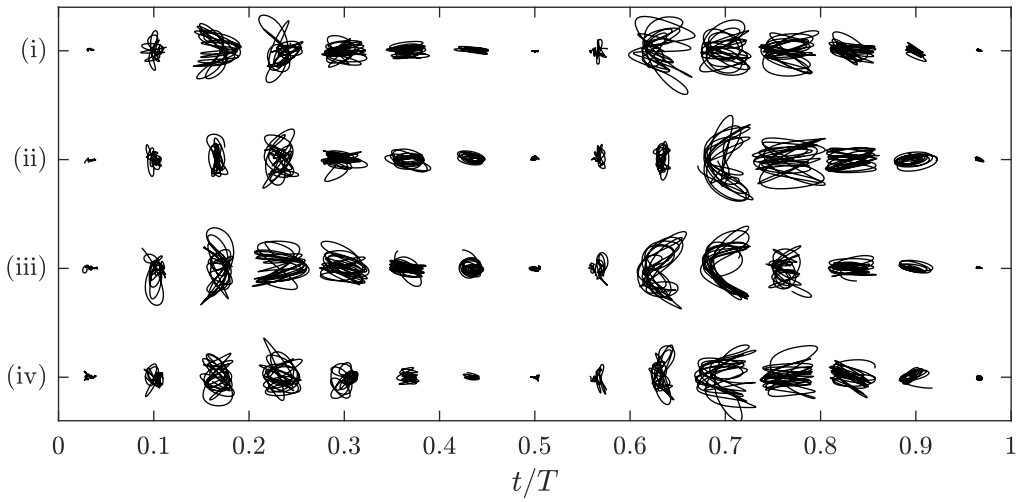

Figure 18: Cylinder vibration through four individual flow-periods in full-array tests for $\hat{U}_r = 2.62$.

substantially between flow periods. Similar chaotic variations were observed for all $\hat{U}_r \geq 1.47$, with no FIV observed for $\hat{U}_r < 1.47$. However, due to the chaotic nature of the trajectories, well-defined regions of each vibration type cannot be clearly identified. Figure 19(a,b) shows the ensemble-averaged vibration amplitudes from the experiments with $\hat{U}_r = 1.47 - 2.74$, with the results for $\hat{U}_r = 2.62$ highlighted as the 'representative' case. Comparing Figure 19(a,b) to Figure 13 shows that the vibration amplitudes from the in-array tests are quite similar those of the isolated cylinder; x-direction vibration amplitudes exhibit strong asymmetry, with much higher amplitudes during flow deceleration than during flow acceleration, while the y-direction amplitudes show little or no asymmetry. For each $\hat{u}_r(t)$, A_x^* for the in-array cylinder is slightly lower compared to the isolated cylinder for the same $u_r(t)$, while A_y^* is slightly higher compared to the isolated cylinder. This can be explained by the more chaotic incident flow for the in-array cylinder compared to the isolated cylinder, including the influence of vortex-shedding from upstream cylinders. Small changes in the incident flow direction causes 'off-axis' in-line and transverse motions; since for the present results $A_x^* > A_y^*$ for most cases, this results in a reduction of A_x^* and an increase in A_y^*.

Figure 19(c) shows ensemble-averaged f_x^* and f_y^* for the full array experiments with $\hat{U}_r = 1.84$ and 2.62, with the dashed line again representing St = 0.2. Due to the chaotic in-array vibrations, consistent frequency estimates can only be obtained within a small section of the flow half-period. When frequency estimates are obtained, they are nearly identical to the frequencies observed for the isolated cylinder (Figure 11). Overall, the results show that, for the set-up with $S_x/d = S_y/d = 6$, FIV of a submerged cylinder within an array can be more chaotic than that for an isolated cylinder, but the average amplitudes and frequencies are similar.

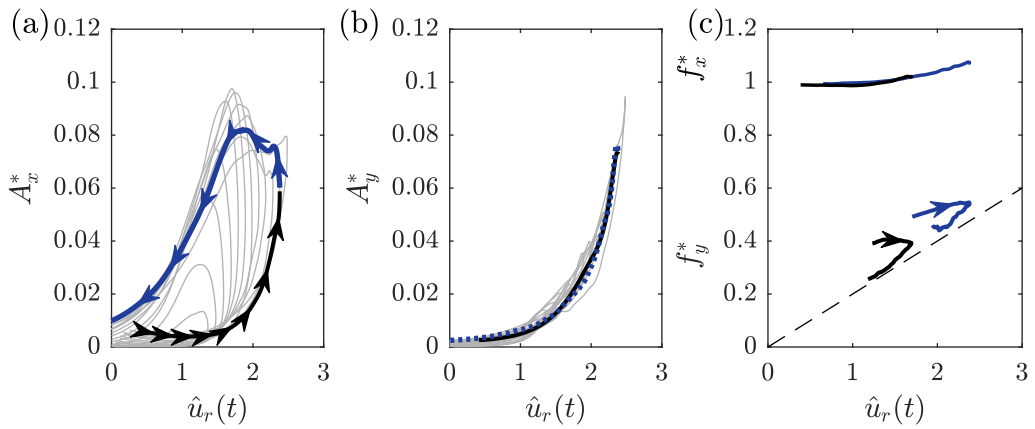

Figure 19: (a,b) Vibration amplitudes in the full-array experiment, with results for $\hat{U}_r = 2.62$ shown in black during flow acceleration and blue during flow deceleration, and all other experiments shown in grey. (c) Vibration frequencies in the full-array experiments for $\hat{U}_r = 1.84$ (black) and 2.62 (blue), with the dashed line representing St = 0.2.

5. Empirical model for in-line vibrations

Section 3.4 shows that A_x^* through the flow half-period exhibits significant hysteresis, particularly for $u_r(t) < 2.5$. To model this unsteady behaviour, Appendix A presents a model for in-line FIV of a single, isolated cylinder in unsteady flow, based on the 'wake-breathing' model of Naudascher (1987). This section will show how, using empirically tuned coefficients, the model in Appendix A can reproduce the unsteady behaviour in A_x^* for the full range of U_r (i.e., not only during in-line vibration). The model is based on the following assumptions: (a) the high-frequency FIV is independent of the low-frequency, quasi-static cylinder deflection; (b) the in-line vibration can be modelled independently of the transverse motion; (c) the influence of 3-D flow characteristics, such as tip vortices, is negligible; and (d) empirical coefficients are constant over the height of the cylinder. Based on the stated assumptions, the in-line vibration is given by:

$$\frac{\mathrm{d}A_x^*}{\mathrm{d}\tau} = -\zeta_{\mathrm{eff}} f_x^* A_x^*, \tag{14a}$$

where $\tau = 2\pi f_{\mathrm{n}} t$ is non-dimensionalised time,

$$f_x^* = \sqrt{1 + \frac{C_2}{2\pi^3 (m^* + C_A)} u_r^2}, \tag{14b}$$

and where:

$$\zeta_{\mathrm{eff}} = f_x^* \cdot \left(\zeta_0 - \frac{C_1 - 2C_0}{2\pi^2 (m^* + C_A)} u_r + \frac{2C_3 \gamma_1}{\pi (m^* + C_A)} f_x^* A_x^* \right), \tag{14c}$$

ζ_{eff} is the 'effective damping ratio', ζ_0 is the still-water damping ratio, C_A is the 'vibration added mass', C_0, C_1, C_2 and C_3 are empirical coefficients, and $\gamma_1 = 0.7389$ is a modal factor to account for the cantilever geometry (Blevins, 1990).

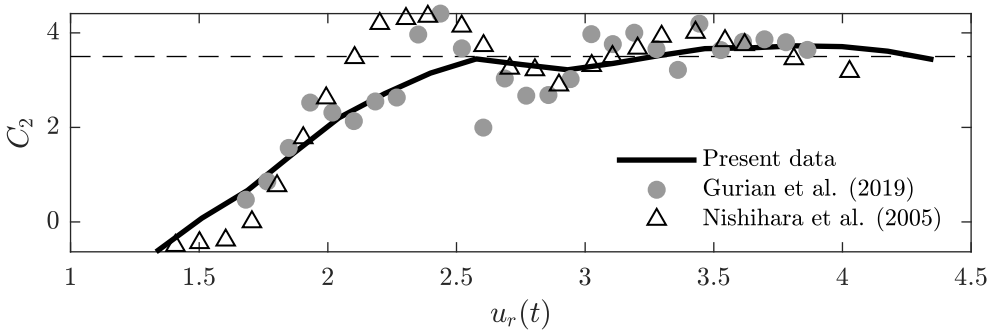

Figure 20: Estimates of C_2 against $u_r(t)$ based on the present data, Gurian et al. (2019) and Nishihara et al. (2005); the dashed line is $C_2 = 3.5$.

Note that the 'vibration added mass', C_A, differs from the 'flow frequency added mass', C_a, discussed in Section 3.1; C_A is a function of the 'vibration KC number' $\mathrm{KC_v} = 2\pi A_x^*$, and since $\mathrm{KC_v} < 1$, $C_A = 1$ is assumed (Sarpkaya, 2004).

C_2 can be obtained from known values of $u_r(t)$ and f_x^* by rearranging Equation (14b). Figure 20 shows C_2 for $0 < u_r(t) < 4.4$ from the present experiments, calculated using the average f_x^* for each $u_r(t)$ (as Figure 11 shows, f_x^* is determined by $u_r(t)$, with no dependence on whether the flow is accelerating or decelerating). Figure 20 shows that C_2 is zero for $u_r(t) < 1.4$, then gradually increases with increasing $u_r(t)$, reaching a near-constant $C_2 = 3.5$ for $u_r(t) > 2.5$ (the dashed line in the figure). Figure 20 also includes values of C_2 inferred from in-line, steady-flow FIV experiments by Gurian et al. (2019), as well as from in-line, steady-flow, forced-vibration experiments by Nishihara et al. (2005), both of which produce similar results to the present data (for the forced-oscillation results of Nishihara et al., 2005, C_2 is inferred from the measured 'effective added-mass' with $f_x^* = 1$). For the present model, we assume $C_2 = 3.5$ for all $u_r(t)$; the difference between measured f_x^* and predicted f_x^* with $C_2 = 3.5$ is small, even for $u_r(t) < 2.5$.

To evaluate C_0, C_1 and C_3, we analyse ζ_eff from the experimental data. First, ζ_eff is calculated from Equation (14a) using the ensemble-averaged measurements of f_x^* and A_x^*. The results for $U_r = 2.57, 3.71, 4.39$ are shown in Figure 21, with the dashed line representing ζ_0. A number of interesting features are seen: for $u_r(t) \lessapprox 1$, all cases show $\zeta_\mathrm{eff} \approx \zeta_0$, implying that vibrations occurring for $u_r(t) < 1$ decay as they would in still water; as $u_r(t)$ increases, ζ_eff becomes increasingly negative, reaches a maximum negative value at $u_r(t) \approx 2$, approaches zero with further increase in $u_r(t)$, before looping back towards ζ_0 as $u_r(t)$ decreases during flow deceleration. We introduce the 'dynamic reduced velocity':

$$u_{r,d}(t) = \frac{u(t)}{f_x(d + 2A_x)} = \frac{u_r(t)}{f_x^*(1 + 2A_x^*)}, \tag{15}$$

which is a reduced velocity defined using dynamic frequency and length scales. The merit of using f_x rather than f_n as the characteristic frequency for u_r has been demonstrated by Khalak and Williamson (1999), who also used the 'apparent projected diameter' $(d + 2A_y)$, introduced by Sarpkaya (1978), as a characteristic length scale for transverse-only vibration; here, for in-line vibrations, we use the corresponding $(d + 2A_x)$. Figure 22 shows $\zeta_\mathrm{eff} - 0.23A_x^*$ plotted against $u_{r,d}(t)$ for all experiments; the 0.23 multiplier was obtained by tuning to give the best collapse of the results

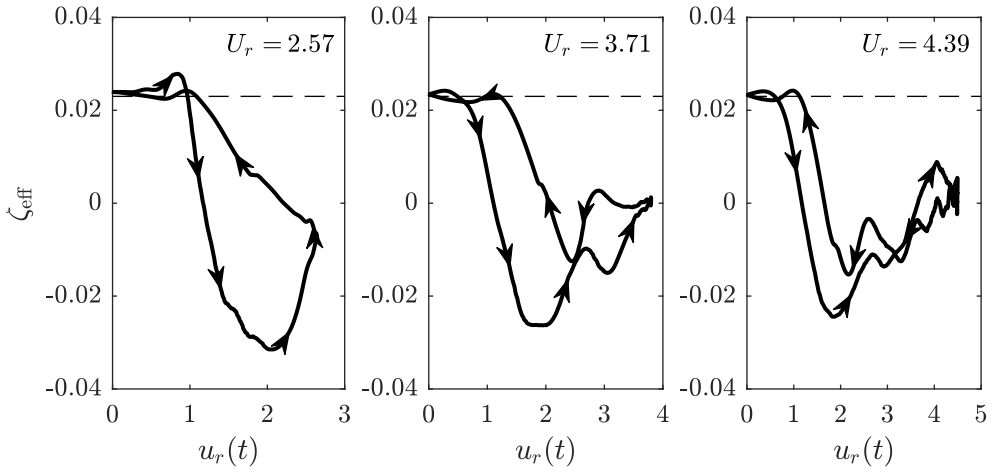

Figure 21: Effective damping for Ur = 2.57, 3.71 and 4.39; the dashed line is the still-water damping ζ_0.

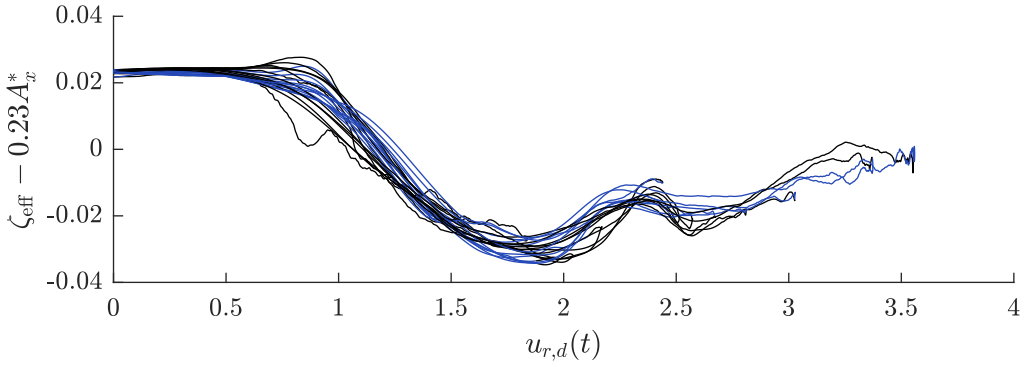

Figure 22: Effective damping $-0.23A_x^*$ against $u_{r,d}(t)$ for all experiments; black/blue lines correspond to accelerating/decelerating stages of the flow half-period.

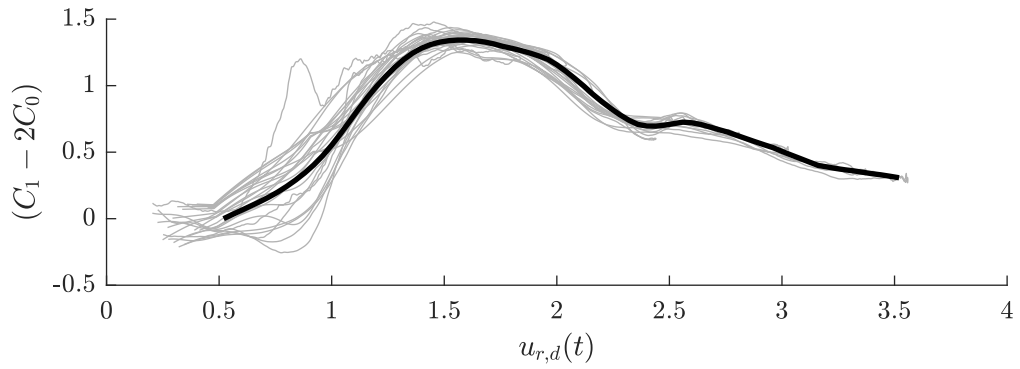

Figure 23: $(C_1 - 2C_0)$ against $u_{r,d}(t)$ with C3=1.5 for $u_r(t) \geq 1$ for all experiments (grey lines); average is shown as the black line.

onto a common curve. The results for accelerating and decelerating flow are shown in black and blue respectively, and are in good agreement. The good collapse of results in Figure 22 indicates that ζ_{eff} may be empirically expressed as the sum of some function of $u_{r,d}(t)$ and a term proportional to A_x^*, i.e.

$$\zeta_{\text{eff}} = \text{f}(u_{r,d}(t)) + \text{C} \cdot A_x^*, \tag{16}$$

which has similar form to Equation (14c). Comparing Equations (14c) and (16) indicates that (a) C_3 has a constant value for $u_r > 1$, and (b) that $(C_1 - 2C_0)$ is a function of $u_{r,d}(t)$. C_3 and $(C_1 - 2C_0)$ are then obtained by empirical fitting: C_3 is constant for $u_r(t) > 1$ and is assumed zero for $u_r(t) < 0.5$ (with a linear transition for $0.5 < u_r(t) < 1$); C_3 is then tuned to give best overlay of $(C_1 - 2C_0)$ versus $u_{r,d}(t)$ across all experiments. The best overlay, obtained with $C_3 = 1.5$, is shown in Figure 23.

The model is applied as follows: A_x^* is given an initial value of 0.002; f_x^* is calculated from the known $u_r(t)$ using Equation (14b) with $C_2 = 3.5$; $u_{r,d}(t)$ is calculated using Equation (15) and $(C_1 - 2C_0)$ is obtained using a look-up based on Figure 23; Equation (14a) and (14c) combine to form a nonlinear ordinary differential equation that is solved (using a constant $C_3 = 1.5$) for A_x^* using the `ode45` function in MATLAB R2018a. Figure 24 shows a comparison between model-predicted and measured vibration amplitudes for the three U_r that represent the three FIV regimes. The comparison shows good agreement, and demonstrates that the model reproduces the unsteady behaviour in A_x^* over the flow half-period very well.

6. Conclusions

In-line and transverse flow-induced vibrations of a cantilevered circular cylinder were measured in large-amplitude, sinusoidal oscillatory flows. Eighteen experiments were conducted for a single, isolated cylinder, with the amplitude of reduced velocity in the range $1.9 \leq U_r \leq 4.4$; the corresponding Reynolds and Keulegan-Carpenter numbers ranged $1300 \leq \text{Re} \leq 10^4$ and $120 \leq \text{KC} \leq 900$ respectively. Forces and moments were measured using a 6-axis load cell, and flow velocities were measured using LDA. The 2-DOF cylinder tip motions were calculated from the measured

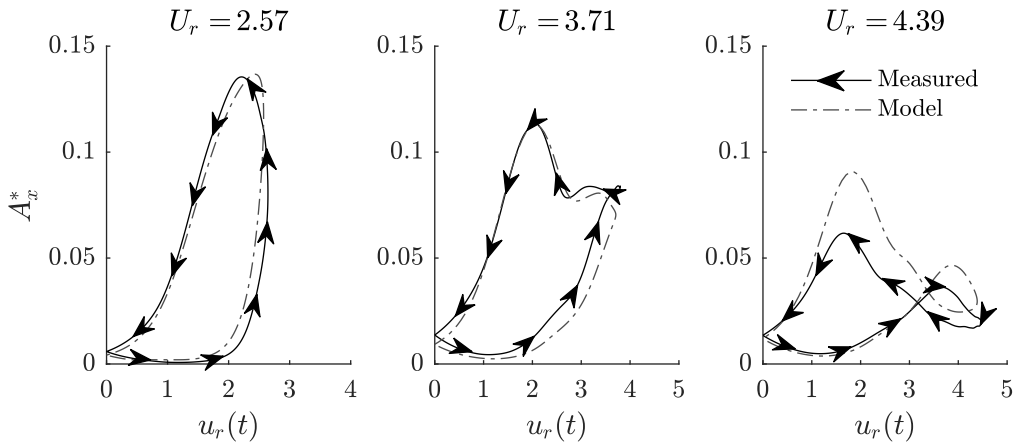

Figure 24: Comparison of model-predicted and measured A_x^* for U_r = 2.57, 3.71 and 4.39.

moments and analysed to determine the vibration trajectories, frequencies and amplitudes. A subsequent set of experiments was carried out in which the instrumented cylinder was placed within a staggered array of similar cylinders with a spacing of six diameters between the cylinders. The following are the main conclusions.

The cylinder undergoes a sequence of vibration responses through a flow half-period. Although the sequence can vary between individual flow half-periods (Figure 6), cosine similarity analysis has shown that a particular sequence dominates for each flow condition. These dominant sequences are presented in a regime diagram showing cylinder tip trajectories for given U_r and given time within the flow period, t/T (Figure 8). The diagram shows that the type of vibrations occurring within the flow half-period depends mainly on U_r, with predominantly in-line vibration occurring for $U_r \lessapprox 2.7$, figure-8 vibration occurring for $2.7 \lessapprox U_r \lessapprox 4$, and transverse vibration occurring for $U_r \gtrapprox 4$. This delineation of vibration type by U_r is in general agreement with observations of FIV in steady flow from previous studies.

Wavelet analysis was used to determine vibration frequencies and amplitudes through the flow half-period. Regardless of vibration type, the in-line vibration frequency, f_x, stays close to the still-water natural frequency ($f_x^* \approx 1$) through the flow half-period, increasing slightly with increasing u_r (Figure 11). f_x shows no unsteady effect, i.e. accelerating flow f_x and decelerating flow f_x are similar for the same u_r. The transverse vibration frequency, f_y, increases as the vortex shedding frequency increases with increasing u_r, and is generally close to the vortex shedding frequency given by St = 0.2. However, here we see some unsteadiness in that, for $u_r \lessapprox 3$, accelerating flow f_y is consistently higher than f_y given by St = 0.2, while the decelerating flow f_y is close to f_y given by St = 0.2.

The most notable unsteady effect is seen in the in-line vibration amplitude, A_x (Figure 13). As the flow accelerates, A_x is at first slow to increase, then increases rapidly for $u_r \gtrapprox 2$. Maximum A_x occurs as the flow decelerates; for all three vibration types, maximum A_x occurs at decelerating $u_r \approx 2$. In contrast to A_x, the transverse vibration amplitudes show little difference between accelerating and decelerating u_r: A_y increases with increasing u_r, reaches a maximum

at maximum u_r, and decreases as the flow decelerates, following the same $A_y - u_r$ dependency as for the accelerating flow. The maximum in-line and transverse vibration amplitudes are found to be in reasonable agreement with vibration amplitudes reported for steady flow FIV (Figure 14); the main differences are that measured values of $A_{x,\max}$ are lower than steady-flow values when $U_r/f^*_{x,\max} < 2$ and higher than steady-flow values when $U_r/f^*_{x,\max} > 2$, both of which are consequences of the aforementioned unsteadiness in A_x. Values of the Lissajous phase for figure-8 vibrations are also found to be in good agreement with steady-flow FIV literature (Figure 15).

For the experiments in which the cylinder is placed within a staggered array with cylinder spacings $S_x/d = S_y/d = 6$, the spatially-averaged horizontal velocities (in the horizontal $x - y$ plane) within the array were found to be depth-uniform and in good agreement with predictions based on Lowe et al. (2005), shown in Figure 17. Cylinder vibrations within the array are more variable between flow periods than those of the isolated cylinder. Nevertheless, the in-array cylinder exhibits very similar averaged vibration characteristics as the isolated cylinder, with similar average vibration amplitudes and frequencies (Figure 19).

Finally, an empirical model has been presented for unsteady in-line vibration based on theoretical considerations and the experimental data. The model assumes that the in-line vibrations are independent of the transverse vibrations and adopts with slight modification the "wake-breathing" forcing proposed by Naudascher (1987). The model comprises an equation for vibration frequency, f_x, for given $u_r(t)$ and a non-linear ordinary differential equation for the vibration amplitude, A_x. The model coefficients are evaluated by fitting to the experimental data, which show consistent behaviour when coefficients are plotted against $u_r(t)$ (for coefficient C_2, which determines f_x) or $u_{r,d}(t)$ (for $C_1 - 2C_0$, which determines the damping). Predicted and measured vibration amplitudes through the flow half-period show very good agreement for in-line, figure-8 and transverse vibration types.

7. Acknowledgements

This work is part of the first author's PhD research funded by the University of Aberdeen. DA acknowledges support from a Royal Society Research Grant (180372). The authors acknowledge the support of the technical staff at the University of Aberdeen, especially Fluids Laboratory Technician Roy Gillanders. The experimental dataset is available on `https://dx.doi.org/10.5281/zenodo.5075188` (will be released upon acceptance of the manuscript).

Aguirre, J. E. (1978). *Flow-induced, in-line vibrations of a circular cylinder*. Doctoral thesis, University of London.

Blevins, R. D. (1990). *Flow induced vibration*. Van Nostrand Reinhold, New York, 2nd edition.

Buchhave, P., George, W. K., and Lumley, J. L. (1979). The measurement of turbulence with the Laser-Doppler Anemometer. *Annual Review of Fluid Mechanics*, 11 (1), pp. 443–503, doi: 10.1146/annurev.fl.11.010179.002303.

Budynas, R. G. and Nisbett, J. K. (2015). *Shigley's mechanical engineering design*. McGraw-Hill.

Cagney, N. and Balabani, S. (2014). Streamwise vortex-induced vibrations of cylinders with one and two degrees of freedom. *Journal of Fluid Mechanics*, 758, pp. 702–727, doi: 10.1017/jfm.2014.521.

Cha, S.-H. (2007). Comprehensive survey on distance/similarity measures between probability density functions. *International Journal of Mathematical Models and Methods in Applied Sciences*, 1 (2), pp. 1.

Feldman, M. (2011). Hilbert transform in vibration analysis. *Mechanical Systems and Signal Processing*, 25 (3), pp. 735–802, doi: 10.1016/j.ymssp.2010.07.018.

Flemming, F. and Williamson, C. H. K. (2005). Vortex-induced vibrations of a pivoted cylinder. *Journal of Fluid Mechanics*, 522, pp. 215–252, doi: 10.1017/S0022112004001831.

Fredsøe, J. and Deigaard, R. (1992). *Mechanics of Coastal Sediment Transport*, volume 3 of *Advanced Series on Ocean Engineering*. World Scientific, Singapore, doi: 10.1142/1546.

Fu, B., Zou, L., and Wan, D. (2018). Numerical study of vortex-induced vibrations of a flexible cylinder in an oscillatory flow. *Journal of Fluids and Structures*, 77, pp. 170–181, doi: 10.1016/j.jfluidstructs.2017.12.006.

Fu, S., Wang, J., Baarholm, R. et al. (2013). Features of vortex-induced vibration in oscillatory flow. *Journal of Offshore Mechanics and Arctic Engineering*, 136 (1), pp. 011801, doi: 10.1115/1.4025759.

Govardhan, R. N. and Williamson, C. H. (2006). Defining the 'modified Griffin plot' in vortex-induced vibration: Revealing the effect of Reynolds number using controlled damping. *Journal of Fluid Mechanics*, 561, pp. 147–180, doi: 10.1017/S0022112006000310.

Gurian, T. D., Currier, T., and Modarres-Sadeghi, Y. (2019). Flow force measurements and the wake transition in purely inline vortex-induced vibration of a circular cylinder. *Physical Review Fluids*, 4 (3), pp. 1–17, doi: 10.1103/PhysRevFluids.4.034701.

Jauvtis, N. and Williamson, C. H. (2004). The effect of two degrees of freedom on vortex-induced vibration at low mass and damping. *Journal of Fluid Mechanics*, 509 (509), pp. 23–62, doi: 10.1017/S0022112004008778.

Jauvtis, N. and Williamson, C. H. K. (2003). Vortex-induced vibration of a cylinder with two degrees of freedom. *Journal of Fluids and Structures*, 17 (7), pp. 1035–1042, doi: 10.1016/S0889-9746(03)00051-3.

Jiang, B., Zhang, X., Xiao, X., and Zhang, L. (2016). Vortex-induced vibration of a tube array with a large pitch-to-diameter ratio value. *Advances in Mechanical Engineering*, 8 (7), pp. 1–16, doi: 10.1177/1687814016654604.

Khalak, A. and Williamson, C. H. K. (1999). Motions, forces and mode transitions in vortex-induced vibrations at low mass-damping. *Journal of Fluids and Structures*, 13 (7-8), pp. 813–851, doi: 10.1006/jfls.1999.0236.

King, R., Prosser, M. J., and Johns, D. J. (1973). On vortex excitation of model piles in water. *Journal of Sound and Vibration*, 29 (2), pp. 169–188, doi: 10.1016/S0022-460X(73)80133-6.

Konstantinidis, E. and Balabani, S. (2007). Symmetric vortex shedding in the near wake of a circular cylinder due to streamwise perturbations. *Journal of Fluids and Structures*, 23 (7), pp. 1047–1063, doi: 10.1016/j.jfluidstructs.2007.03.002.

Konstantinidis, E. (2014). On the response and wake modes of a cylinder undergoing streamwise vortex-induced vibration. *Journal of Fluids and Structures*, 45, pp. 256–262, doi: 10.1016/j.jfluidstructs.2013.11.013.

Konstantinidis, E., Dorogi, D., and Baranyi, L. (2021). Resonance in vortex-induced in-line vibration at low Reynolds numbers. *Journal of Fluid Mechanics*, 907, pp. A34, doi: 10.1017/jfm.2020.850.

Kühtz, S. (1996). *Experimental Investigation of Oscillatory Flow around circular cylinders at low β numbers*. Doctoral thesis, Imperial College London (University of London).

Lipsett, A. W. and Williamson, I. D. (1994). Response of a cylinder in oscillatory flow. *Journal of Fluids and Structures*, 8 (7), pp. 681–709, doi: 10.1016/S0889-9746(94)90160-0.

Lowe, R. J., Koseff, J. R., and Monismith, S. G. (2005). Oscillatory flow through submerged canopies: 1. Velocity structure. *Journal of Geophysical Research C: Oceans*, 110 (10), pp. 1–17, doi: 10.1029/2004JC002788.

Naudascher, E. (1987). Flow-induced streamwise vibrations of structures. *Journal of Fluids and Structures*, 1 (3), pp. 265–298, doi: 10.1016/0889-9746(87)90243-X.

Nishihara, T., Kaneko, S., and Watanabe, T. (2005). Characteristics of fluid dynamic forces acting on a circular cylinder oscillated in the streamwise direction and its wake patterns. *Journal of Fluids and Structures*, 20 (4 SPEC. ISS.), pp. 505–518, doi: 10.1016/j.jfluidstructs.2005.02.003.

Oengören, A. and Ziada, S. (1998). An in-depth study of vortex shedding, acoustic resonance and turbulent forces in normal triangle tube arrays. *Journal of Fluids and Structures*, 12 (6), pp. 717–758, doi: 10.1006/jfls.1998.0162.

Okajima, A., Nakamura, A., Kosugi, T. et al. (2004). Flow-induced in-line oscillation of a circular cylinder. *European Journal of Mechanics -*

B/Fluids, 23 (1), pp. 115–125, doi: 10.1016/j.euromechflu.2003.09.009.

Païdoussis, M. (1983). A review of flow-induced vibrations in reactors and reactor components. *Nuclear Engineering and Design*, 74 (1), pp. 31–60, doi: 10.1016/0029-5493(83)90138-3.

Pesce, C. P. and Fujarra, A. L. C. (2000). Vortex-induced vibrations and jump phenomenon: Experiments with a clamped flexible cylinder in water. *International Journal of Offshore and Polar Engineering*, 10 (1), pp. 26–33, doi: 10.3390/rel2010077.

Sarpkaya, T. (1976). In - Line And Transverse Forces, On Cylinders In Oscillatory Flow At High Reynolds Numbers. *Offshore Technology Conference*, (c), pp. 96–108, doi: 10.4043/2533-MS.

Sarpkaya, T. (1978). Fluid Forces on Oscillating Cylinders. *Journal of the Waterway, Port, Coastal and Ocean Division*, 104 (3), pp. 275–290, doi: 10.1061/JWPCDX.0000101.

Sarpkaya, T. (1995). Hydrodynamic Damping, Flow-Induced Oscillations, and Biharmonic Response. *Journal of Offshore Mechanics and Arctic Engineering*, 117 (4), pp. 232–238, doi: 10.1115/1.2827228.

Sarpkaya, T. (2004). A critical review of the intrinsic nature of vortex-induced vibrations. *Journal of Fluids and Structures*, 19 (4), pp. 389–447, doi: 10.1016/j.jfluidstructs.2004.02.005.

Sarpkaya, T. (2005). On the parameter β=Re/KC=D2/νT. *Journal of Fluids and Structures*, 21 (4), pp. 435–440, doi: 10.1016/j.jfluidstructs.2005.08.007.

Schlichting, H. and Gersten, K. (2017). *Boundary-layer theory*. Springer, Berlin, Heidelberg, doi: 10.1007/978-3-662-52919-5.

Strømmen, E. N. (2014). *Structural Dynamics*, volume 2 of *Springer Series in Solid and Structural Mechanics*. Springer International Publishing, Cham, doi: 10.1007/978-3-319-01802-7.

Sumer, B. M. and Fredsøe, J. (2006). *Hydrodynamics around cylindrical structures*, volume 26 of *Advanced Series on Ocean Engineering*. World Scientific, Singapore, doi: 10.1142/6248.

Tanida, Y., Okajima, A., and Watanabe, Y. (1973). Stability of a circular cylinder oscillating in uniform flow or in a wake. *Journal of Fluid Mechanics*, 61 (4), pp. 769–784, doi: 10.1017/S0022112073000935.

Thorsen, M. J., Sævik, S., and Larsen, C. M. (2016). Time domain simulation of vortex-induced vibrations in stationary and oscillating flows. *Journal of Fluids and Structures*, 61, pp. 1–19, doi: 10.1016/j.jfluidstructs.2015.11.006.

Wang, C., Ren, W. X., Wang, Z. C., and Zhu, H. P. (2013). Instantaneous frequency identification of time-varying structures by continuous wavelet transform. *Engineering Structures*, 52, pp. 17–25, doi: 10.1016/j.engstruct.2013.02.006.

Williamson, C. H. and Roshko, A. (1988). Vortex formation in the wake of an oscillating cylinder. *Journal of Fluids and Structures*, 2 (4), pp. 355–381, doi: 10.1016/S0889-9746(88)90058-8.

Williamson, C. H. K. and Govardhan, R. (2004). Vortex-induced vibrations. *Annual Review of Fluid Mechanics*, 36 (1), pp. 413–455, doi: 10.1146/annurev.fluid.36.050802.122128.

Zhao, M. (2013). Numerical investigation of two-degree-of-freedom vortex-induced vibration of a circular cylinder in oscillatory flow. *Journal of Fluids and Structures*, 39, pp. 41–59, doi: 10.1016/j.jfluidstructs.2013.02.003.

Zhao, M., Cheng, L., An, H., and Tong, F. (2015). Flow and flow-induced vibration of a square array of cylinders in steady currents. *Fluid Dynamics Research*, 47 (4), doi: 10.1088/0169-5983/47/4/045505.

Appendix A. 1-DOF unsteady in-line FIV model

The governing equation describing the motion of the cantilever is obtained from Euler-Bernoulli beam theory:

$$m\ddot{r}_x + c\dot{r}_x + EI\frac{\partial^4 r_x}{\partial z^4} = F_x(z,t), \tag{A.1}$$

where m and c are structural mass and damping per unit length, E is Young's modulus, I is second moment of area, $r_x(z,t)$ is the cylinder deflection, F_x is forcing along x, and the dot represents a time-derivative. As stated in

Section 2.2, cylinder deflection is taken as the linear sum of a quasi-static deflection and a dynamic deflection; we assume that, at a given time, the cylinder motion takes the form:

$$r_x = r_{x,0}(z,t) + r'_x(z,t) \simeq r_{x,0}(z,t) + a_x(z,t)\sin(\omega_x t), \tag{A.2a}$$

where $r_{x,0}(z,t)$ is the quasi-static motion, $r'_x(z,t)$ is the dynamic motion, $a_x(z,t)$ is the amplitude of vibration at any z, and $\omega_x = 2\pi f_x$ is the angular frequency of vibration. Since the flow is unsteady, values of $r_{x,0}$, a_x and ω_x can all vary in time. For the conditions of the present experiments, the frequency of vibration is much higher than the rate of change in these values, i.e. $\left|\dot{r}_{x,0}\right| \ll \omega_x a_x$, $|\dot{a}_x| \ll \omega_x a_x$ and $|\dot{\omega}_x| \ll \omega_x^2$. Hence, over short time intervals, $r_{x,0}$, a_x and ω_x can be considered constant, and we have:

$$\dot{r}_x \simeq \omega_x a_x \cos(\omega_x t) \tag{A.2b}$$

$$\ddot{r}_x \simeq -\omega_x^2 a_x \sin(\omega_x t), \tag{A.2c}$$

Dynamic deflections are assumed to occur solely in the first flexural mode (see Section 2.2), with the deflection shape resembling the first eigenmode of a uniform cantilever in free, undamped vibration, i.e.:

$$r'_x(z,t) = \bar{\phi}_1(z)X(t) \tag{A.3a}$$

$$a_x(z,t) = \bar{\phi}_1(z)A_x, \tag{A.3b}$$

where $X(t)$ denotes the dynamic tip deflection, and $\bar{\phi}_1(z) = \phi_1(z)/\phi_1^{\max}$ is the normalised deflection shape. ϕ_1 denotes the first eigenmode of a cantilever:

$$\phi_1(\bar{z}) = \frac{\sin\alpha_1 - \sinh\alpha_1}{\cos\alpha_1 + \cosh\alpha_1}(\sin\alpha_1\bar{z} - \sinh\alpha_1\bar{z}) + \cos\alpha_1\bar{z} - \cosh\alpha_1\bar{z} \tag{A.4}$$

where $\alpha_1 = 1.8751$, and where $\bar{z} = (z + 5\,\text{mm})/L$ is the non-dimensional vertical coordinate, with L denoting the cylinder length (measured from the base at $z = -5$ mm). Force in Equation (A.1) is given by the Morison equation (in relative-velocity form):

$$F_x(z,t) = \frac{1}{2}\rho C_D d \cdot (u - \dot{r}_x)\,|u - \dot{r}_x| + C_A\frac{\rho\pi d^2}{4}(\dot{u} - \ddot{r}_x) + \frac{\rho\pi d^2}{4}\dot{u}, \tag{A.5}$$

This can be simplified if $(u - \dot{r}_x) \geq 0$, which is generally true at all times unless (a) vibration is forced, or (b) flow velocity has recently reduced, and oscillations are still dissipating. The impact of the latter is minimal, and the drag-term in Equation (A.5) can therefore be simplified as:

$$F_D = \frac{1}{2}\rho d u^2 C_D\left(1 - \frac{\dot{r}_x}{u}\right)^2 \tag{A.6}$$

Based on Naudascher (1987), we propose the following dynamic C_D formulation:

$$C_D = C_0 + C_1\frac{\dot{r}_x}{u} - C_2\frac{r'_x}{d} + C_3\frac{\omega_x a_x}{u}, \tag{A.7}$$

where C_0 represents the component of C_D which is unaffected by the in-line vibration, C_1 and C_2 represent in-phase and out-of-phase components of the fluctuating drag, and C_3 represents the increase in mean drag with increasing vibration amplitude. Each term in Equation (A.7) has been non-dimensionalised by the most intuitively relevant characteristic scales (C_1 and C_3 are the primary forcing terms, and their normalisation is based on the significance of the ratio $\dot{r}_x/u$ described by Naudascher (1987), whereas the out-of-phase term C_2 is simply normalised by d). Using Equation (A.2c), the C_2-term can be re-formulated by substituting $\ddot{r}_x = -\omega_x^2 r'_x$. Inserting Equation (A.7) into Equation (A.6) and expanding produces a number of steady terms, some terms oscillating at f_x, and some higher-order terms oscillating at $2f_x$ and $3f_x$ which can be neglected, resulting in the following expression for total drag force:

$$F_D = \frac{1}{2}\rho d u^2 \left(C_0 + C_3 \frac{\omega_x a_x}{u} + \left(C_0 - 2C_1 + C_3 \frac{\omega_x a_x}{u} \right) \frac{\omega_x^2 a_x^2}{2u^2} + \left(\left(1 + \frac{3\omega_x^2 a_x^2}{4u^2} \right) C_1 - 2C_0 - 2C_3 \lambda \right) \frac{\dot{r}_x}{u} + \left(1 + \frac{\omega_x^2 a_x^2}{4u^2} \right) C_2 \frac{\ddot{r}_x}{\omega_x^2 d} \right) \tag{A.8}$$

By assuming linear stiffness, the quasi-static terms are subtracted from both sides of Equation (A.1), and the governing equation for the dynamic cylinder motion becomes:

$$m\ddot{r}_x + c\dot{r}_x + EI\frac{\partial^4 r'_x}{\partial z^4} = \frac{\rho d u}{2}\left((C_1 - 2C_0) - 2C_3 \frac{\omega_x a_x}{u} + \frac{3C_1 \omega_x^2 a_x^2}{4u^2} \right) \dot{r}_x - \frac{\rho \pi d^2}{4}\left(C_a - \frac{2C_2 u^2}{\pi \omega_x^2 d^2}\left(1 + \frac{\omega_x^2 a_x^2}{4u^2} \right) \right) \ddot{r}_x \tag{A.9}$$

Applying principles of modal analysis (Blevins, 1990), all terms in Equation (A.9) are multiplied by ϕ_1 before integrating over $\bar{z}$ and dividing by $\int_0^1 \phi_1^2 \mathrm{d}\bar{z}$, resulting in:

$$m\ddot{X} + c\dot{X} + kX = \frac{\rho d u}{2}\left((C_1 - 2C_0) - 2C_3 \gamma_1 \lambda + \frac{3C_1 \gamma_2 \lambda^2}{4} \right) \dot{X} - \frac{\rho \pi d^2}{4}\left(C_a - \frac{2C_2 u^2}{\pi \omega_x^2 d^2}\left(1 + \frac{\gamma_2 \lambda^2}{4} \right) \right) \ddot{X} \tag{A.10}$$

where λ is the non-dimensional ratio of cylinder tip velocity amplitude to flow velocity:

$$\lambda = \frac{\omega_x A_x}{u}, \tag{A.11}$$

and where the following modal parameters have been introduced:

$$\gamma_1 = \frac{\int_0^1 \phi_1^3 \mathrm{d}\bar{z}}{\int_0^1 \phi_1^2 \mathrm{d}\bar{z}} = 0.7389 \tag{A.12a}$$

$$\gamma_2 = \frac{\int_0^1 \phi_1^4 \mathrm{d}\bar{z}}{\int_0^1 \phi_1^2 \mathrm{d}\bar{z}} = 0.5872 \tag{A.12b}$$

$$k = EI\frac{\int_0^1 \phi_1 \frac{\mathrm{d}^4 \phi_1}{\mathrm{d}z^4} \mathrm{d}\bar{z}}{\int_0^1 \phi_1^2 \mathrm{d}\bar{z}} = \frac{\alpha_1^4 EI}{L^4} \tag{A.12c}$$

Equation (A.10) can also be represented as:

$$(m + m_{EA})\ddot{X} + (c + c_a)\dot{X} + kX = 0, \tag{A.13}$$

which resembles the equation for free vibration of a damped harmonic oscillator. The 'effective added mass' is $m_{EA} = C_{EA} \cdot \rho \pi d^2/4$, with the effective added-mass coefficient C_{EA} obtained from Equation (A.10):

$$C_{EA} = C_A - \frac{C_2 u_r^2}{2\pi^3 f_x^{*2}}\left(1 + \frac{1}{4}\gamma_2 \lambda^2 \right), \tag{A.14}$$

The 'added-damping' c_a is also obtained from Equation (A.10):

$$c_a = \frac{\rho d u}{2}\left(2C_0 + 2C_3\gamma_1\lambda - \left(1 + \frac{3}{4}\gamma_2\lambda^2\right)C_1\right) \tag{A.15}$$

Over short intervals, the solution of Equation (A.13) takes the form of an underdamped harmonic oscillator:

$$X(t+\delta t) = A_x(t)e^{-\zeta_{\text{eff}}\omega_x\delta t}\sin(\omega_x\delta t + \theta_t), \tag{A.16}$$

where θ_t is the vibration phase at time t, and where ζ_{eff} is the effective damping ratio, given by:

$$\zeta_{\text{eff}} = \frac{c + c_a}{2\omega_x\,(m + m_{EA})} \tag{A.17}$$

Hence, the rate of change in amplitude is given by:

$$\frac{\mathrm{d}A_x}{\mathrm{d}t} = -\zeta_{\text{eff}}\omega_x A_x(t) \tag{A.18}$$

Since the natural frequency of a cylinder in still water is $\omega_{\text{n}} = \sqrt{k/(m+m_A)}$, while the vibration frequency during FIV is $\omega_x = \sqrt{k/(m+m_{EA})}$, the frequency ratio can be found as:

$$f_x^* = \frac{\omega_x}{\omega_{\text{n}}} = \sqrt{\frac{m^* + C_A}{m^* + C_A - \frac{C_2 u_r^2}{2\pi^3 f_x^{*2}}\left(1 + \frac{1}{4}\gamma_2\lambda^2\right)}}, \tag{A.19}$$

which can be rewritten as:

$$f_x^* = \sqrt{1 + \frac{1 + \frac{1}{4}\gamma_2\lambda^2}{2\pi^3\,(m^* + C_A)}C_2 u_r^2}, \tag{A.20}$$

Inserting the still-water damping ratio $\zeta_0 = c/2\omega_{\text{n}}(m + m_A)$ in Equation (A.17), and non-dimensionalising in terms of u_r, m^* and f_x^* yields the following expression for effective damping:

$$\frac{\zeta_{\text{eff}}}{f_x^*} = \zeta_0 - \frac{C_1\left(1 + \frac{3}{4}\gamma_2\lambda^2\right) - 2C_0}{2\pi^2(m^* + C_a)}u_r + \frac{2C_3\gamma_1}{\pi(m^* + C_a)}f_x^* A_x^* \tag{A.21}$$

The terms in Equations (A.20) and (A.21) which are proportional to λ^2 are problematic from a modelling perspective, as they can create positive-feedback loops. To remove this issue, the model is linearised by substituting $C_1' = C_1\left(1 + \frac{3}{4}\gamma_2\lambda^2\right)$ and $C_2' = C_2\left(1 + \frac{1}{4}\gamma_2\lambda^2\right)$. Since λ is generally small ($\lambda \leq 0.4$ in the present results for $u_r(t) > 0.5$), variations in C_1' and C_2' are small, and in most cases, $C_1' \approx C_1$ and $C_2' \approx C_2$. The simplified model equations then become:

$$f_x^* = \sqrt{1 + \frac{C_2}{2\pi^3\,(m^* + C_A)}u_r^2} \tag{A.22a}$$

$$\frac{\zeta_{\text{eff}}}{f_x^*} = \zeta_0 - \frac{C_1 - 2C_0}{2\pi^2\,(m^* + C_A)}u_r + \frac{2C_3\gamma_1}{\pi\,(m^* + C_A)}f^* A_x^*, \tag{A.22b}$$

Equation (A.18) is non-dimensionalised by introducing the non-dimensional time $\tau = 2\pi f_{\text{n}} t$:

$$\frac{\mathrm{d}A_x^*}{\mathrm{d}\tau} = -\zeta_{\text{eff}} f_x^* A_x^* \tag{A.22c}$$